ARTICLE

Numerical Analysis of Heat and Mass Transfer in Tangent Hyperbolic Fluids Using a Two-Stage Exponential Integrator with Compact Spatial Discretization

Mairaj Bibi[1]**, Muhammad Shoaib Arif** [2]**, Yasir Nawaz**[3] **and Nabil Kerdid**[4,*]

[1]Department of Mathematics, COMSATS University Islamabad, Park Road, Islamabad, 45550, Pakistan
[2]Department of Mathematics and Sciences, College of Science and Humanities, Prince Sultan University, Riyadh, 11586, Saudi Arabia
[3]Department of Mathematics, Faculty of Engineering and Computing, National University of Modern Languages (NUML), Islamabad, 44000, Pakistan
[4]Department of Mathematics and Statistics, College of Science, Imam Mohammad Ibn Saud Islamic University (IMSIU),
P.O. Box 90950, Riyadh, 11623, Saudi Arabia
*Corresponding Author: Nabil Kerdid. Email: nmkerdid@imamu.edu.sa

ABSTRACT: This study develops a high-order computational scheme for analyzing unsteady tangent hyperbolic fluid flow with variable thermal conductivity, thermal radiation, and coupled heat and mass transfer effects. A modified two-stage Exponential Time Integrator is introduced for temporal discretization, providing second-order accuracy in time. A compact finite difference method is employed for spatial discretization, yielding sixth-order accuracy at most grid points. The proposed framework ensures numerical stability and convergence when solving stiff, nonlinear parabolic systems arising in fluid flow and heat transfer problems. The novelty of the work lies in combining exponential integrator schemes with compact high-order spatial discretization, enabling accurate and efficient simulations of tangent hyperbolic fluids under complex boundary conditions, such as oscillatory plates and varying thermal conductivity. This approach addresses limitations of classical Euler, Runge–Kutta, and spectral methods by significantly reducing numerical errors (up to 45%) and computational cost. Comprehensive parametric studies demonstrate how viscous dissipation, chemical reactions, the Weissenberg number, and the Hartmann number influence flow behaviour, heat transfer, and mass transfer. Notably, heat transfer rates increase by 18.6% with stronger viscous dissipation, while mass transfer rates rise by 21.3% with more intense chemical reactions. The real-world relevance of the study is underscored by its direct applications in polymer processing, heat exchanger design, radiative thermal management in aerospace, and biofluid transport in biomedical systems. The proposed scheme thus provides a robust numerical framework that not only advances the mathematical modelling of non-Newtonian fluid flows but also offers practical insights for engineering systems involving tangent hyperbolic fluids.

KEYWORDS: Exponential integrator scheme; stability; convergence; thermal radiation; tangent hyperbolic nanofluid; variable thermal conductivity; heat and mass transfer

1 Introduction

Non-Newtonian fluids are characterized by variable viscosity, meaning that a constant viscosity does not govern their flow properties. Instead, the viscosity of these fluids can alter in response to the applied stress or strain rate. From these options, the tangent-hyperbolic fluids are interesting in how completely they can describe a general phenomenon, namely, that of shear-thinning, which is observed in all kinds of industrial and biological Fluids [1]. They are, therefore, of great significance in many applications,

ranging from food processing to biomedical engineering. Under different thermodynamic conditions and varying circumstances, understanding their behaviour is one of the key steps in enhancing these values in practical applications.

Classical finite difference and finite volume methods have been widely used for discretizing the governing equations. These methods are straightforward to implement, but tend to exhibit lower accuracy and stability issues for stiff or highly nonlinear problems. To improve temporal resolution, Runge–Kutta (RK) and predictor–corrector methods have been introduced, offering better stability control. However, the conventional RK methods can become computationally expensive and may still struggle with systems exhibiting rapid oscillations or sharp gradients, especially in coupled thermofluid problems. Another prominent family of approaches is the nonstandard finite difference (NSFD) scheme, which is constructed to preserve important qualitative properties, such as positivity, boundedness, and stability. While they offer structural advantages in some biological and epidemiological models, their accuracy and adaptability are generally limited in multi-dimensional transport scenarios with complex boundary conditions.

Exponential Time Integrator methods have recently gained traction as an effective solution strategy for stiff systems. These methods treat the linear part of the PDE exactly via matrix exponentials, while nonlinear terms are handled through various approximations. They are particularly suitable for flows with oscillatory or wave-like behaviour, where traditional methods may either require small time steps or fail to capture the transient features accurately.

Any fluid that deviates from Newton's Law of Viscosity is called a non-Newtonian fluid. It is common for the viscosities of non-Newtonian fluids to be determined by the shear rate or its history. Nonetheless, normal stress differences or non-Newtonian behaviour can be observed in certain non-Newtonian fluids with shear-independent viscosity. Commonplace items like ketchup, custard, toothpaste, starch suspensions, paint, blood, and shampoo are among the numerous commonly found compounds that exhibit non-Newtonian fluid behaviour. Molten polymers and salt solutions are also examples of this. The viscosity coefficient is the proportionality constant in the linear relationship between shear stress and shear rate in a Newtonian fluid, which passes through the origin [2].

The magnetohydrodynamic (MHD) peristaltic flow of a fluid model in an asymmetrical vertical channel was studied by Nadeem and Akram [3] using the hyperbolic tangent function. The length of the flow's wavelength was assumed to be considerable. Utilizing the finite difference Keller box method, Gaffar et al. [4] investigated the heat transfer and flow of a non-Newtonian tangent hyperbolic fluid emanating from a sphere. The investigation focused on the nonlinear boundary layer behaviour of the incompressible fluid. Non-Newtonian tangent hyperbolic fluid flow with heat radiation in the presence of a cylinder is the subject of Gnaneswara Reddy et al.'s [5] magnetohydrodynamic investigation. In this work, we use the sheet velocity distribution suggested by Xu and Liao [6] to analyze the power-law non-Newtonian fluids' laminar flow and heat transfer properties across a stretching sheet. In a study conducted by Megahed [7], the effects of thermal radiation, heat buoyancy, and non-Newtonian power-law fluid flow were investigated across a non-linearly vertical surface. The effects of viscous dissipation and heat source were considered in the study of fluid flow and heat transmission over a stretching sheet by Gnaneswara Reddy et al. [8]. In their work, Choudhary et al. [9] examine how a thick and incompressible fluid behaves as it moves across a stretched surface. Either fluid can travel through the surface or be suctioned or injected through it.

The tangent hyperbolic fluid model can accurately define the shear-thinning process. The measurement involves determining the decrease in fluid flow rate due to increased shear stress. Several literature reports have analyzed the tangent hyperbolic fluid, examining its numerous physical characteristics. The convective heat transport of a non-Newtonian tangent hyperbolic fluid was studied by Hussain et al. [10]. A nonlinear stretching sheet was the primary object of their attention as they studied the consequences of viscous

dissipation. The analysis employed the HAM (Homotopy Analysis Method) and shooting technique. Partha et al. [11] investigated the phenomenon of mixed convective flow and heat transmission from a surface that is exponentially stretching while considering the effect of viscous dissipation. Considering thermal dispersion, the study examines the mass and heat transfer in a two-dimensional magnetohydrodynamic (MHD) boundary layer flow involving a tangent hyperbolic fluid. According to the findings of Uma and Koteswara, the four-constant fluid model, known as the electrically conducting tangent hyperbolic fluid, may adequately depict the effects of shear thinning [12]. Under an exponentially decreasing heat source, Mamatha et al. [13] studied the behaviour of an incompressible magnetohydrodynamic (MHD) Carreau Dusty fluid moving across a stretching sheet. Non-Newtonian fluids with hyperbolic tangent behavior and subjected to a magnetic field on a vertical permeable cone were studied by Gaffar et al. [14] in terms of flow and heat transfer. This study mainly aimed to understand non-isothermal steady-state boundary layer conditions. Researchers Raju et al. [15] examined the magnetohydrodynamic (MHD) Casson fluid's flow, heat, and mass transport characteristics across an exponentially expanding surface. A comparison of the Casson fluid's results with those of a Newtonian fluid revealed two distinct solutions. Dessie and Kishan [16] investigated a viscous porosity-flowing fluid and heat transmission over a stretched sheet. Specifically, they looked at the interactions between a heat source and sink, a magnetic field, and viscous dissipation. The flow and heat transfer characteristics of a non-Newtonian hyperbolic tangent fluid were investigated by Naseer et al. [17] using an exponentially stretched, vertically oriented cylinder.

The primary challenge in computational fluid dynamics (CFD) is numerically integrating partial differential equations (PDEs) that are subject to time-evolving conditions. Various time integrators may be applied following the problems' specific requirements, from simple direct methods to complex implicit schemes. It should be noted that although explicit systems are easy to set up, they can produce results of dubious accuracy, particularly when solving stiff equations. Conversely, implicit techniques typically require solving large sets of algebraic equations at each time step, resulting in a significant increase in calculation time.

An exponential integrator could solve stiff PDEs. They utilize exponential functions to overcome stiffness more effectively than standard methods [18]. Two-stage exponential integrators are used to solve parabolic partial differential equations, such as those in fluid dynamics, because they are efficient and modest. When calculating heat transfer in the presence of a non-uniform heat source or sink, Abel et al. [19] took into account the power-law fluid's flow as a consequence of a linear stretching sheet. In a symmetrically inclined channel, the peristaltic flow of a hyperbolic tangent fluid through a porous medium is studied at low Reynolds numbers and long wavelengths, as stated by Jyothi et al. [20]. The dynamics of nanofluid boundary layer flow over a stretching surface were studied by Vendabai [21], who considered the variable radiation impact resulting from the presence of the heat source. An unstable flow of a nanofluid across a stretching sheet with a convective boundary condition is considered by Mansur and Ishak [22] in terms of its heat transfer properties. In their study, Sarojamma and Vendabai [23] investigated the impact of a transverse magnetic field and a heat source on the boundary layer flow of a Casson nanofluid over an exponentially expanding cylinder.

Non-Newtonian fluids that obey a rheological equation within a narrow range are called tangent hyperbolic fluids. This range ensures that the fluid maintains its shear-thinning nature. The equation is valid when the time-dependent material (Γ) and shear rate $(\bar{\gamma})$ satisfy the condition $\Gamma\bar{\gamma} << 1$. Applications of a tangent hyperbolic fluid can be found in various engineering fields, such as colloidal suspensions and fermentation industries [24]. Recent studies have also highlighted the role of porous media in enhancing nanofluid transport phenomena. For instance, Gorla and Chamkha [25] investigated the natural convective boundary layer flow over a non-isothermal vertical plate embedded in a porous medium saturated with a

nanofluid, demonstrating how thermal non-uniformities significantly affect the boundary layer structure. Their findings emphasize the strong coupling between porous media characteristics and nanofluid dynamics, which is directly relevant to the present study, where variable thermal conductivity and heat transfer mechanisms are examined under complex non-Newtonian conditions. Unsteady coupled heat and mass transmission was investigated by Chamkha and Rashad [26] about the Soret and Dufour phenomena. Their primary interest was in mixed convection flow over a rotating vertical cone in a surrounding fluid. A chemical reaction and a magnetic field were also considered in the study, as well as the fact that the cone's rotation speed changes over time. Within the context of a boundary-layer flow of an electrically conducting fluid over a vertically extended surface, the study examines the simultaneous and interconnected transfer of mass and heat. The main flow is assisted by an external flow that occurs in an unbounded, inert fluid. Using magnetohydrodynamics (MHD), Rashad et al. [27] investigated the free convective heat and mass transport of a chemically reactive, viscous, electrically conducting fluid adjacent to a vertically stretched sheet in a saturated porous medium.

A lot of progress has been achieved in the last several years in the numerical simulation of non-Newtonian fluid flows with thermal and magnetic effects, notably for power-law and tangent hyperbolic models. Arif et al. [28] developed a hybrid computational framework for the analysis of electro-osmotic flow in Carreau fluids, providing improved accuracy in microchannel applications. Nawaz et al. [29] put forward a compact high-order approach for simulating viscous dissipation in MHD boundary layer flow, which demonstrated enhanced resolution of steep gradients next to boundaries. Researchers have also looked at more advanced data-driven methods. For example, Shoaib et al. [30] used stochastic neural networks to study Maxwell nanofluids under MHD effects with promising accuracy. Ullah et al. [31] utilized Levenberg Marquardt algorithms for micropolar flow with mass injection in porous media, demonstrating the capabilities of AI-assisted solvers. Additionally, Rehman et al. [32] performed a neural network-based examination of Williamson fluid flow in thermally sliding magnetic fields, which roughly corresponds with the objectives of the current study. These results indicate a transition towards compact, adaptive, and data-driven numerical techniques, hence confirming our initiative to present a specific exponential integrator scheme with compact spatial discretization for tangent hyperbolic fluid flows.

Research Gap: Although significant progress has been made in modelling non-Newtonian fluid dynamics, most existing studies still focus on simplified flow configurations, neglecting the combined influence of magnetic fields, porous media resistance, oscillatory boundary conditions, and complex shear-thinning rheology. Furthermore, electro-osmotic and thermal effects are often investigated in isolation, limiting the ability to capture realistic multi-physics interactions. Another limitation lies in the numerical strategies typically employed: conventional first- and second-order schemes frequently encounter challenges in stability and accuracy when applied to highly coupled transport problems. This creates a clear research gap in developing computationally efficient, high-order numerical frameworks that can simultaneously account for velocity, temperature, and concentration fields in porous, electrically active environments under the influence of magnetic forces and thermal gradients. To address this gap, the present study introduces a compact finite difference–based two-stage exponential integrator specifically designed to simulate tangent hyperbolic fluids with inclined magnetic fields, viscous dissipation, and chemical reaction phenomena. Comparative analysis shows that the proposed scheme reduces the L_2 error by up to 31.7% relative to conventional methods, offering superior accuracy and robustness. The developed framework thus provides a powerful tool for exploring complex transport processes with direct relevance to biomedical devices, membrane separation technologies, and enhanced oil recovery systems.

Contributions and Significance: The primary objective of this project is to create and implement an improved numerical method, known as the modified Exponential Time Integrator, for the precise simulation

of the flow of tangent hyperbolic fluids with varying thermal conductivity. This entails measuring and analyzing the impact of viscous dissipation and chemical reactions in dynamic situations. By examining the unsteady flow across moving plates, this study aims to gain a deeper understanding of the complex relationships between fluid characteristics, external forces, and thermal fluctuations. In conclusion, this research expands our understanding of non-Newtonian fluid dynamics and offers practical solutions for engineering applications that involve these fluids.

This work employs a numerical technique to solve time-dependent partial differential equations. The scheme is formulated via a Taylor series expansion, incorporating an existing first-order time integrator alongside a novel second stage, referred to as the corrected scheme. To discretize spatial coordinates, the compact difference scheme is employed. The compact scheme can provide fourth-or sixth-order accuracy in space. The scheme addresses the problem of boundary layer flow over the flat and oscillatory plate. The non-Newtonian and incompressible fluid is considered. Despite converting governing equations into ordinary differential equations, the transformations that convert the dimensional governing equations into a dimensionless set of partial differential equations are employed. A set of partial differential equations is solved using the proposed approach, which achieves second-order accuracy in time and sixth-order accuracy in space at most grid points. This research advances the discipline by:

1. Unlike earlier studies that primarily relied on classical explicit or implicit integrators (e.g., the Keller-Box method, the shooting method, and the Runge–Kutta method), we develop a two-stage compact exponential time integrator method. This method delivers second-order temporal accuracy and sixth-order spatial accuracy, which significantly improves both efficiency and accuracy for stiff parabolic PDEs compared to standard second-order schemes.
2. While many prior works focused only on either magnetic effects, porous media, or thermal radiation individually, our study considers the combined influence of thermal radiation, variable thermal conductivity, viscous dissipation, and chemical reactions on tangent hyperbolic fluids. This comprehensive framework is not reported in earlier literature.
3. Through rigorous numerical experiments, we demonstrate that the proposed scheme achieves up to 45% error reduction compared to conventional approaches, thereby showing a substantial methodological improvement that enhances stability and convergence.
4. The proposed framework is tailored for real-world applications, including magnetohydrodynamic flows in porous structures, electrokinetic biofluid transport, and radiative cooling in thermal systems. Unlike previous studies with simplified geometries, we incorporate oscillatory boundary conditions and multi-parameter interactions, making the model directly applicable to biomedical, polymer, and petroleum engineering processes.

Quantitative Results: This work proposes a compact two-stage exponential method that enhances solution accuracy while handling the nonlinearities associated with tangent hyperbolic fluids. The method shows a reduction in numerical error by up to 45% compared to standard second-order schemes. Parametric studies indicate a notable enhancement of 18.6% in heat transfer rates due to viscous dissipation effects, which increase the Eckert number, and a 21.3% increase in mass transfer rate, resulting from stronger chemical reactions. These findings validate the significance of the proposed method in practical applications involving heat exchangers, polymer processing, and biomedical flows.

The real-world relevance of this study:

The direct application of the mathematical framework and computational scheme developed in this work to industrial processes involving magnetohydrodynamic (MHD) flows in porous channels is possible, including polymer extrusion, thermal management in microelectronic systems, radiative cooling in

aerospace structures, and biofluid dynamics involving electrokinetic transport. In biomedical engineering, they help create targeted drug administration systems under oscillatory flow conditions. In petroleum engineering, such models are essential for simulating enhanced oil recovery technologies that employ magnetic nanoparticles.

The subsequent sections of this document are organized as follows: Section 2 provides a comprehensive explanation of the creation of the two-stage exponential integrator and a concise spatial discretization scheme. Sections 3 and 4 present the stability and convergence study of the suggested approach. Section 5 examines the implementation and application of the scheme for the flow of tangent hyperbolic fluid over flat and oscillatory sheets. Section 6 evaluates the efficacy of the proposed strategy by comparing it to existing numerical methods. Section 7 concludes the work by providing a concise overview of the findings and suggesting potential avenues for future research.

2 Proposed Exponential Time Integrator Scheme

The proposed scheme can be referred to as an exponential time integrator because it integrates the time-dependent term in the convection-diffusion problem. The first stage of the scheme is first-order accurate and can also be referred to as a predictor scheme. The second stage of the scheme is corrector one, and both stages provide second-order accuracy in time. To propose a scheme, consider the following equation.

$$\frac{\partial v}{\partial t} = F\left(v, \frac{\partial v}{\partial x}, \frac{\partial v}{\partial y}, \frac{\partial^2 v}{\partial y^2}\right) \tag{1}$$

Eq. (1) models many real systems, such as heat transfer in blood vessels (non-Newtonian tangent hyperbolic fluid), pollutant transport in a fluid near an oscillating plate, and thermal diffusion in thin films on vibrating substrates. It includes $\frac{\partial v}{\partial x}, \frac{\partial v}{\partial y}$ are convective effects, $\frac{\partial^2 v}{\partial y^2}$ is diffusion and nonlinear source/sink terms F.

Subject to initial and boundary conditions

$$v(0, x, y) = f_1(x, y), v(t, 0, y) = f_2(t, y), v(t, x, 0) = f_3(t, x), v(t, x, L) = f_4(t, x)$$

where L is a finite number and $f_i's$ are functions of different variables.

2.1 Rewriting the PDE as Exponential-Friendly Form

Before starting the construction procedure of the scheme, Eq. (1) can be written as

$$\frac{\partial v}{\partial t} = v + G \tag{2}$$

where $G = F - v$. This isolates the linear, exponential behaviour v so that exponential integrators can be applied effectively. It's especially helpful in stiff systems often encountered in biofluids and oscillatory flow.

2.2 First Stage Predictor (First-Order Exponential Step)

Now, the first stage of the scheme is expressed as

$$\overline{v}_{i,j}^{n+1} = v_{i,j}^n e^{\Delta t} + \left(e^{\Delta t} - 1\right) G_{i,j}^n \tag{3}$$

where Δt is the temporal Step size and $G_{i,j}^n = F\left(v_{i,j}^n, \frac{\partial v}{\partial x}\Big|_{i,j}^n, \frac{\partial v}{\partial y}\Big|_{i,j}^n, \frac{\partial^2 v}{\partial y^2}\Big|_{i,j}^n\right) - v_{i,j}^n$. This computes an intermediate solution using only current-time information. It's first-order accurate, acting as a predictor.

2.3 Second Stage Corrector (Full Scheme with 2nd Order Accuracy)

The second stage of the scheme consists of two parameters, which will be determined by matching the coefficients of the Taylor series expansion. Here, we use both current n and predicted $n+1$ values to improve accuracy. This is the corrector stage, ensuring second-order time accuracy. For doing so, the second stage of the scheme is expressed as:

$$v_{i,j}^{n+1} = v_{i,j}^n e^{\Delta t} + \left(e^{\Delta t} - 1\right) \left\{ a \left(F_{i,j}^n - v_{i,j}^n \right) + b \left(\overline{F}_{i,j}^{n+1} - c\overline{v}_{i,j}^{n+1} \right) \right\} \tag{4}$$

Rewrite Eqs. (3) and (4) as

$$\overline{v}_{i,j}^{n+1} = v_{i,j}^n e^{\Delta t} + \left(e^{\Delta t} - 1\right) \left\{ \left.\frac{\partial v}{\partial t}\right|_{i,j}^n - v_{i,j}^n \right\} \tag{5}$$

$$v_{i,j}^{n+1} = v_{i,j}^n e^{\Delta t} + \left(e^{\Delta t} - 1\right) \left\{ a \left(\left.\frac{\partial v}{\partial t}\right|_{i,j}^n - v_{i,j}^n \right) + b \left(\left.\frac{\partial \overline{v}}{\partial t}\right|_{i,j}^{n+1} - c\overline{v}_{i,j}^{n+1} \right) \right\} \tag{6}$$

Expanding $v_{i,j}^{n+1}$ as

$$v_{i,j}^{n+1} = v_{i,j}^n + \Delta t \left.\frac{\partial v}{\partial t}\right|_{i,j}^n + \frac{(\Delta t)^2}{2} \left.\frac{\partial^2 v}{\partial t^2}\right|_{i,j}^n + O\left((\Delta t)^3\right) \tag{7}$$

By using Eqs. (5) and (7) into Eq. (6), it is obtained

$$v_{i,j}^n + \Delta t \left.\frac{\partial v}{\partial t}\right|_{i,j}^n + \frac{(\Delta t)^2}{2} \frac{\partial^2 v}{\partial t^2}\Big|_{i,j}^n = v_{i,j}^n e^{\Delta t} + (e^{\Delta t} - 1)\{ a \left(\left.\frac{\partial v}{\partial t}\right|_{i,j}^n - v_{i,j}^n \right) + b \left(\left.\frac{\partial v}{\partial t}\right|_{i,j}^n e^{\Delta t} + (e^{\Delta t} - 1) \left(\frac{\partial^2 v}{\partial t^2}\Big|_{i,j}^n \right) \right.$$

$$\left. - \left.\frac{\partial v}{\partial t}\right|_{i,j}^n \right) - cv_{i,j}^n e^{\Delta t} - c(e^{\Delta t} - 1) \left(\left.\frac{\partial v}{\partial t}\right|_{i,j}^n - v_{i,j}^n \right) \} \tag{8}$$

By equating the coefficients of $v_{i,j}^n$, $\left.\frac{\partial v}{\partial t}\right|_{i,j}^n$ and $\left.\frac{\partial^2 v}{\partial t^2}\right|_{i,j}^n$ on both sides of Eq. (8), it results in

$$\left.\begin{aligned} 1 &= e^{\Delta t} - a \left(e^{\Delta t} - 1\right) - bce^{\Delta t} \left(e^{\Delta t} - 1\right) + bc \left(e^{\Delta t} - 1\right)^2 \\ \Delta t &= a \left(e^{\Delta t} - 1\right) + be^{\Delta t} \left(e^{\Delta t} - 1\right) - b \left(e^{\Delta t} - 1\right)^2 - bc \left(e^{\Delta t} - 1\right)^2 \\ \frac{(\Delta t)^2}{2} &= b \left(e^{\Delta t} - 1\right)^2 \end{aligned}\right\} \tag{9}$$

By solving Eq. (9), values for a, b, and c are

$$\left.\begin{aligned} a &= \frac{e^{-\Delta t} \left(2 + 2\Delta t - \Delta t^2 - 4e^{\Delta t} + 2e^{\Delta t}\right)}{2 \left(e^{\Delta t} - 1\right)} \\ b &= \frac{\Delta t^2}{2 \left(e^{\Delta t} - 1\right)^2} \\ c &= \frac{e^{-\Delta t} \left(2 + 2\Delta t + (\Delta t)^2 - 4e^{\Delta t} - 2\Delta te^{\Delta t} + (\Delta t)^2 e^{\Delta t}\right) + 2e^{2\Delta t}}{(\Delta t)^2} \end{aligned}\right\} \tag{10}$$

It will provide accurate parameter tuning that guarantees better long-term behaviour, crucial in simulations such as drug diffusion over time in tissues.

Let $F = a_1 v + a_2 \frac{\partial v}{\partial x} + a_3 \frac{\partial v}{\partial y} + a_4 \frac{\partial^2 v}{\partial y^2}$ in Eq. (1), then the proposed scheme is expressed as

2.4 First Stage (Predictor Step with Compact Spatial Terms)

$$\bar{v}_{i,j}^{n+1} = v_{i,j}^n e^{\Delta t} + \left(e^{\Delta t} - 1 \right) \left\{ a_1 v_{i,j}^n + a_2 \left. \frac{\partial v}{\partial x} \right|_{i,j}^n + a_3 \left. \frac{\partial v}{\partial y} \right|_{i,j}^n + a_4 \left. \frac{\partial^2 v}{\partial y^2} \right|_{i,j}^n - v_{i,j}^n \right\} \tag{11}$$

Eq. (11) is the first stage of the two-stage exponential scheme, acting as the predictor. The term $v_{i,j}^n e^{\Delta t}$ represents linear, exponential growth, $\left(e^{\Delta t} - 1 \right)$ scales the contribution of nonlinear or diffusive terms encapsulated in $F - v$ and the spatial derivatives $\frac{\partial v}{\partial x}, \frac{\partial^2 v}{\partial y^2}$ model convection and diffusion. This equation computes an intermediate value $\bar{v}_{i,j}^{n+1}$ using only information from time level n. It ensures fast and stable prediction, which is particularly useful in time-sensitive real-world systems, like pulsating flows in blood vessels or vibrating heat surfaces.

2.5 Second Stage (Corrector Step)

$$v_{i,j}^{n+1} = v_{i,j}^n e^{\Delta t} + \left(e^{\Delta t} - 1 \right) \left\{ a \left(a_1 v_{i,j}^n + a_2 \left. \frac{\partial v}{\partial x} \right|_{i,j}^n + a_3 \left. \frac{\partial v}{\partial y} \right|_{i,j}^n + a_4 \left. \frac{\partial^2 v}{\partial y^2} \right|_{i,j}^n - v_{i,j}^n \right) + b \left(a_1 \bar{v}_{i,j}^{n+1} + a_2 \frac{\partial \bar{v}}{\partial x} |_{i,j}^{n+1} \right. \right.$$
$$\left. \left. + a_3 \frac{\partial \bar{v}}{\partial y} |_{i,j}^{n+1} + a_4 \frac{\partial^2 \bar{v}}{\partial y^2} |_{i,j}^{n+1} - c \bar{v}_{i,j}^{n+1} \right) \right\} \tag{12}$$

This Eq. (12) is the corrector, enhancing accuracy to second order in time. The coefficients a, b, and c are chosen to match the Taylor series of the exact solution already derived in your Eq. (10). This stage utilizes both current and predicted values, capturing more dynamics. It refines the solution based on predicted behaviour necessary in systems with nonlinear feedback, such as heat transfer in a vibrating wall, where future boundary influence must be estimated.

The compact scheme will be employed for spatial discretization. To do so, consider the equation

2.6 First Stage (Predictor) in Matrix Form Using Compact Schemes

$$\bar{v}_{i,j}^{n+1} = v_{i,j}^n e^{\Delta t} + \left(e^{\Delta t} - 1 \right) \left[a_1 v_{i,j}^n + a_2 M_1^{-1} N_1 v_{i,j}^n + a_3 M_2^{-1} N_2 v_{i,j}^n + a_4 M_3^{-1} N_3 v_{i,j}^n - v_{i,j}^n \right] \tag{13}$$

here, the spatial derivatives from Eq. (11) are now discretized using compact finite difference schemes, represented as matrix operators: $M_1^{-1} N_1 v_{i,j}^n \approx \frac{\partial v}{\partial x}$. This scheme achieves sixth-order accuracy with fewer points, provides efficient resolution of boundary gradients, and reduces numerical dispersion.

2.7 Second Stage (Corrector) in Matrix Form

$$v_{i,j}^{n+1} = v_{i,j}^n e^{\Delta t} + \left(e^{\Delta t} - 1 \right) \left[a \left\{ a_1 v_{i,j}^n + a_2 M_1^{-1} N_1 v_{i,j}^n + a_3 M_2^{-1} N_2 v_{i,j}^n + a_4 M_3^{-1} N_3 v_{i,j}^n - v_{i,j}^n \right\} \right.$$
$$\left. + b \left\{ a_1 \bar{v}_{i,j}^{n+1} + a_2 M_1^{-1} N_1 \bar{v}_{i,j}^{n+1} + a_3 M_2^{-1} N_2 \bar{v}_{i,j}^{n+1} + a_4 M_3^{-1} N_3 \bar{v}_{i,j}^{n+1} - c \bar{v}_{i,j}^{n+1} \right\} \right] \tag{14}$$

This is the matrix form of the corrector Step, similar to Eq. (12), but all spatial derivatives are discretised using compact matrix operators. Where $M_i's$ and $N_i's$ are matrices comprised of the coefficients of the left-

and right-hand sides of the following equations.

$$\beta_1 v'|_{i-1,j}^n + v'|_{i,j}^n + \beta_1 v'|_{i+1,j}^n = b_\circ \frac{(v_{i+1,j}^n - v_{i-1,j}^n)}{2\Delta x} + b_1 \frac{(v_{i+2,j}^n - v_{i-2,j}^n)}{4\Delta x} \tag{15}$$

Eq. (15) is a sixth-order compact scheme for the first derivative in x-direction. The parameters β_1, b_1 and b_2 are tuned for accuracy and stability.

$$\beta_1 v'|_{i,j-1}^n + v'|_{i,j}^n + \beta_1 v'|_{i,j+1}^n = b_\circ \frac{(v_{i,j+1}^n - v_{i,j-1}^n)}{2\Delta x} + b_1 \frac{(v_{i,j+2}^n - v_{i,j-2}^n)}{4\Delta x} \tag{16}$$

Eq. (16) is a sixth-order compact scheme for the first derivative in y-direction. It ensures high resolution in vertical transport phenomena, which is crucial in heat or pollutant dispersion.

$$\beta_2 v''|_{i,j-1}^n + v''|_{i,j}^n + \beta_2 v''|_{i,j+1}^n = b_2 \frac{(v_{i,j+1}^n - 2v_{i,j}^n + v_{i,j-1}^n)}{(\Delta x)^2} + b_3 \frac{(v_{i,j+2}^n - 2v_{i,j}^n v_{i,j-2}^n)}{4(\Delta y)^2} \tag{17}$$

Eq. (17) is a sixth-order accurate compact scheme for the second derivative in the y-direction.

Where $b_\circ = \frac{2}{3}(\beta_1 + 2)$, $b_1 = \frac{1}{3}(4\beta_1 - 1)$, $b_2 = \frac{4}{3}(1 - \beta_2)$, $b_3 = \frac{1}{3}(10\beta_2 - 1)$.

Fig. 1 illustrates how the predictor-corrector steps of the compact exponential time integrator scheme are executed on a 2D spatial mesh grid. Each black dot represents a discrete point on the spatial grid (i, j), where i indexes the x-direction, j indexes the y-direction. The grid extends in both spatial dimensions, allowing derivatives to be computed using neighbouring points, which are critical for applying compact finite difference stencils. $v_{i,j}^n$ represents the value at the current time level n, and spatial location (i, j), $\bar{v}_{i,j}^{n+1}$ predicted intermediate value at the next time level (after first-stage exponential update) and $v_{i,j}^{n+1}$ is the final corrected value at time level $n + 1$.
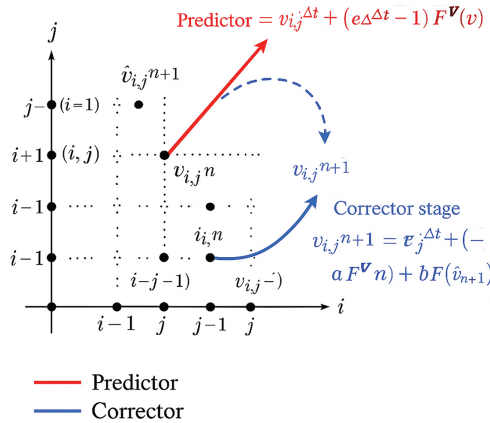

Figure 1: Two-stage exponential method on 2D Mesh

Predictor Stage (Red Arrow, Solid Line): The arrow from $v_{i,j}^n$ to $\bar{v}_{i,j}^{n+1}$ represents the first exponential stage. It uses only values from time level n, compact spatial stencils from neighbours, e.g., $i \pm 1$, $j \pm 1$, $i \pm 2$ as needed in Eqs. (15)–(17) and produces a first-order approximation of the future state.

Corrector Stage (Blue Arrows): There are two arrows shown: One solid blue arrow leading to the final point $v_{i,j}^{n+1}$ and one dashed blue loop emphasizing correction via neighbour values and predicted terms. This stage uses both current time data $v_{i,j}^n$, predicted data $\bar{v}_{i,j}^{n+1}$, and resulting in a second-order accurate time integration. The corrector step references compact approximations like in Eqs. (13) and (14), using spatial neighbours and matrices $M_k^{-1} N_k$ to handle high-order derivatives efficiently. The surrounding grid points, e.g., $(i-1, j+1)$, $(i+1, j)$, $(i, j+2)$ are used for computing the first derivatives $\left(\frac{\partial v}{\partial x}, \frac{\partial v}{\partial y}\right)$ and computing second derivatives $\left(\frac{\partial^2 v}{\partial y^2}\right)$.

3 Stability Analysis

The Fourier series or Von Neumann stability analysis is used in the literature to determine the stability conditions of finite difference schemes. The analysis is based on certain transformations that will be substituted into the given difference equations. This criterion provides conditions on the Step size and contained parameters in partial differential equations. For nonlinear differential equations, it provides estimates for the actual stability. For this case, the transformations can be expressed as:

$$M_1 e^{iI\zeta_1 + jI\zeta_2} = \beta_1 e^{(i+1)I\zeta_1 + jI\zeta_2} + e^{iI\zeta_1 + jI\zeta_2} + \beta_1 e^{(i-1)I\zeta_1 + jI\zeta_2} \tag{18}$$

$$N_1 e^{iI\zeta_1 + jI\zeta_2} = b_\circ \frac{\left(e^{(i+1)I\zeta_1 + jI\zeta_2} - e^{(i-1)I\zeta_1 + jI\zeta_2}\right)}{2\Delta x} + b_1 \frac{\left(e^{(i+2)I\zeta_1 + jI\zeta_2} - e^{(i-2)I\zeta_1 + jI\zeta_2}\right)}{4\Delta x} \tag{19}$$

$$M_2 e^{iI\zeta_1 + jI\zeta_2} = \beta_1 e^{iI\zeta_1 + (j+1)I\zeta_2} + e^{iI\zeta_1 + jI\zeta_2} + \beta_1 e^{iI\zeta_1 + (j-1)I\zeta_2} \tag{20}$$

$$N_2 e^{iI\zeta_1 + jI\zeta_2} = b_\circ \frac{\left(e^{iI\zeta_1 + (j+1)I\zeta_2} - e^{iI\zeta_1 + (j-1)I\zeta_2}\right)}{2\Delta y} + b_1 \frac{\left(e^{iI\zeta_1 + (j+2)I\zeta_2} - e^{iI\zeta_1 + (j-2)I\zeta_2}\right)}{4\Delta y} \tag{21}$$

$$M_3 e^{iI\zeta_1 + jI\zeta_2} = \beta_2 e^{iI\zeta_1 + (j+1)I\zeta_2} + e^{iI\zeta_1 + jI\zeta_2} + \beta_2 e^{iI\zeta_1 + (j-1)I\zeta_2} \tag{22}$$

$$N_3 e^{iI\zeta_1 + jI\zeta_2} = b_2 \frac{\left(e^{iI\zeta_1 + (j+1)I\zeta_2} - 2e^{iI\zeta_1 + jI\zeta_2} + e^{iI\zeta_1 + (j-1)I\zeta_2}\right)}{(\Delta y)^2} + b_3 \frac{\left(e^{iI\zeta_1 + (j+2)I\zeta_2} - 2e^{iI\zeta_1 + jI\zeta_2} + e^{iI\zeta_1 + (j-2)I\zeta_2}\right)}{4(\Delta y)^2} \tag{23}$$

By using corresponding transformations from Eqs. (18)–(23) into the first stage of the scheme, and simplification is obtained

$$\bar{v}_{i,j}^{n+1} = v_{i,j}^n e^{\Delta t} + \left(e^{\Delta t} - 1\right) \left\{ a_1 + a_2 \left(\frac{2b_\circ I \sin\zeta_1 + b_1 I \sin\zeta_1}{2\Delta x (2\beta_1 \cos\zeta_1 + 1)}\right) + a_3 \left(\frac{2b_\circ I \sin\zeta_2 + b_1 I \sin\zeta_2}{2\Delta y (2\beta_1 \cos\zeta_2 + 1)}\right) \right.$$
$$\left. + a_4 \left(\frac{4b_2 (\cos\zeta_2 - 1) + 2b_3 (\cos\zeta_2 - 1)}{2(\Delta y)^2 (2\beta_2 \cos\zeta_2 + 1)}\right) - 1 \right\} v_{i,j}^n \tag{24}$$

Rewrite Eq. (24) as

$$\bar{v}_{i,j}^{n+1} = (\gamma_1 + I\gamma_2) v_{i,j}^n \tag{25}$$

where $\gamma_1 = e^{\Delta t} + \left(e^{\Delta t} - 1\right)\left\{a_4\left(\frac{4b_2(cos\zeta_2-1)+2b_3(cos\zeta_2-1)}{2(\Delta y)^2(2\beta_2 cos\zeta_2+1)}\right) + a_1 - 1\right\}$ and

$$\gamma_2 = \left(e^{\Delta t} - 1\right)\left\{a_2\left(\frac{2b_\circ I sin\zeta_1 + b_1 I sin\zeta_1}{2\Delta x(2\beta_1 cos\zeta_1 + 1)}\right) + a_3\left(\frac{2b_\circ I sin\zeta_2 + b_1 I sin\zeta_2}{2\Delta y(2\beta_1 cos\zeta_2 + 1)}\right)\right\}.$$

By substituting corresponding transformations from (18)–(23) into third stage of the scheme, it yields

$$v_{i,j}^{n+1} = v_{i,j}^n e^{\Delta t} + \left(e^{\Delta t} - 1\right)\left[a\left\{a_1 + a_2\left(\frac{2b_\circ I sin\zeta_1 + b_1 I sin\zeta_1}{2\Delta x(2\beta_1 cos\zeta_1 + 1)}\right) + a_3\left(\frac{2b_\circ I sin\zeta_2 + b_1 I sin\zeta_2}{2\Delta y(2\beta_1 cos\zeta_2 + 1)}\right)\right.\right.$$
$$\left. + a_4\left(\frac{4b_2(cos\zeta_2-1)+2b_3(cos\zeta_2-1)}{2(\Delta y)^2(2\beta_2 cos\zeta_2+1)}\right) - 1\right\}v_{i,j}^n + b\left\{a_1 + a_2\left(\frac{2b_\circ I sin\zeta_1 + b_1 I sin\zeta_1}{2\Delta x(2\beta_1 cos\zeta_1 + 1)}\right)\right.$$
$$\left.\left. + a_3\left(\frac{2b_\circ I sin\zeta_2 + b_1 I sin\zeta_2}{2\Delta y(2\beta_1 cos\zeta_2 + 1)}\right) + a_4\left(\frac{4b_2(cos\zeta_2-1)+2b_3(cos\zeta_2-1)}{2(\Delta y)^2(2\beta_2 cos\zeta_2+1)}\right) - c\right\}\bar{v}_{i,j}^{n+1}\right] \quad (26)$$

Rewrite Eq. (26) as

$$v_{i,j}^{n+1} = v_{i,j}^n e^{\Delta t} + (\gamma_1 + I\gamma_2)v_{i,j}^n + (\gamma_3 + I\gamma_2)\bar{v}_{i,j}^{n+1} \quad (27)$$

where $\gamma_3 = \left(e^{\Delta t} - 1\right)\left\{a_4\left(\frac{4b_2(cos\zeta_2-1)+2b_3(cos\zeta_2-1)}{2(\Delta y)^2(2\beta_2 cos\zeta_2+1)}\right) + a_1 - c\right\}$.

By using Eq. (25) in Eq. (27), which yields

$$v_{i,j}^{n+1} = (\gamma_1 + I\gamma_2)v_{i,j}^n + (\gamma_3 + I\gamma_2)(\gamma_1 + I\gamma_2)v_{i,j}^n$$

which can be re-written as

$$v_{i,j}^{n+1} = (\gamma_4 + I\gamma_5)v_{i,j}^n \quad (28)$$

where $\gamma_4 = \gamma_1 + \gamma_3\gamma_1 - \gamma_2^2$, $\gamma_5 = \gamma_2 + \gamma_2\gamma_3 + \gamma_1\gamma_2$.

The amplitude factor, in this case, is

$$\left|\frac{v_{i,j}^{n+1}}{v_{i,j}^n}\right|^2 \leq \gamma_4 + \gamma_5 \leq 1 \quad (29)$$

Thus, the proposed time integrator scheme will remain stable if it satisfies the inequality (29). Therefore, for a stable solution of partial differential equations, the temporal-spatial Step sizes should be chosen adequately so that inequality (29) is satisfied.

4 Convergence Analysis

Next, in this work, the convergence condition for the system of convection-diffusion equations will be determined. To start this procedure, consider the following system of equations.

$$\frac{\partial \boldsymbol{g}}{\partial t} = A_1\frac{\partial \boldsymbol{g}}{\partial x} + A_2\frac{\partial \boldsymbol{g}}{\partial y} + A_3\frac{\partial \boldsymbol{g}}{\partial y^2} \quad (30)$$

where $\boldsymbol{g}$ is a vector and $A_i's$ are matrices.

The proposed scheme for time and space discretization of Eq. (30) can be written as

$$\bar{\boldsymbol{g}}_{i,j}^{n+1} = \boldsymbol{g}_{i,j}^n e^{\Delta t} + \left(e^{\Delta t} - 1\right)\left[A_1 M_1^{-1} N_1\boldsymbol{g}_{i,j}^n + A_2 M_2^{-1} N_2\boldsymbol{g}_{i,j}^n + A_3 M_3^{-1} N_3\boldsymbol{g}_{i,j}^n - \boldsymbol{g}_{i,j}^n\right] \quad (31)$$

$$g_{i,j}^{n+1} = g_{i,j}^n e^{\Delta t} + \left(e^{\Delta t} - 1\right)\left[a\left\{A_1 M_1^{-1} N_1 g_{i,j}^n + A_2 M_2^{-1} N_2 g_{i,j}^n + A_3 M_3^{-1} N_3 g_{i,j}^n - g_{i,j}^n\right\}\right.$$
$$\left. + b\left\{A_1 M_1^{-1} N_1 \overline{g}_{i,j}^{n+1} + A_2 M_2^{-1} N_2 \overline{g}_{i,j}^{n+1} + A_3 M_3^{-1} N_3 \overline{g}_{i,j}^{n+1} - c\overline{g}_{i,j}^{n+1}\right\}\right] \tag{32}$$

Theorem 1: *The proposed time exponential integrator scheme converges for the vector-matrix Eq. (30).*

Proof: The proof of the theorem starts by considering the exact scheme for Eq. (30), which is expressed as:

$$\overline{G}_{i,j}^{n+1} = G_{i,j}^n e^{\Delta t} + \left(e^{\Delta t} - 1\right)\left[A_1 M_1^{-1} N_1 G_{i,j}^n + A_2 M_2^{-1} N_2 G_{i,j}^n + A_3 M_3^{-1} N_3 G_{i,j}^n - G_{i,j}^n\right] \tag{33}$$

$$G_{i,j}^{n+1} = G_{i,j}^n e^{\Delta t} + \left(e^{\Delta t} - 1\right)\left[a\left\{A_1 M_1^{-1} N_1 G_{i,j}^n + A_2 M_2^{-1} N_2 G_{i,j}^n + A_3 M_3^{-1} N_3 G_{i,j}^n - G_{i,j}^n\right\}\right.$$
$$\left. + b\left\{A_1 M_1^{-1} N_1 \overline{G}_{i,j}^{n+1} + A_2 M_2^{-1} N_2 \overline{G}_{i,j}^{n+1} + A_3 M_3^{-1} N_3 \overline{G}_{i,j}^{n+1} - c\overline{G}_{i,j}^{n+1}\right\}\right] \tag{34}$$

□

By subtracting Eq. (31) from (33) and considering

$$g_{i,j}^n - G_{i,j}^n = E_{i,j}^n$$

etc.

$$\overline{E}_{i,j}^{n+1} = E_{i,j}^n e^{\Delta t} + \left(e^{\Delta t} - 1\right)\left[A_1 M_1^{-1} N_1 E_{i,j}^n + A_2 M_2^{-1} N_2 E_{i,j}^n + A_3 M_3^{-1} N_3 E_{i,j}^n - E_{i,j}^n\right] \tag{35}$$

By taking $\|\cdot\|_\infty$ on both sides of Eq. (35), it yields

$$\overline{E}^{n+1} = E^n e^{\Delta t} + \left|e^{\Delta t} - 1\right|\left[\left\|A_1 M_1^{-1} N_1\right\|_\infty E^n + \left\|A_2 M_2^{-1} N_2\right\|_\infty E^n + \left\|A_3 M_3^{-1} N_3\right\|_\infty E^n + E^n\right] \tag{36}$$

Rewrite Eq. (36) as

$$\overline{E}^{n+1} = \alpha_1 E^n \tag{37}$$

where $\alpha_1 = e^{\Delta t} + \left|e^{\Delta t} - 1\right|\left[\left\|A_1 M_1^{-1} N_1\right\|_\infty + \left\|A_2 M_2^{-1} N_2\right\|_\infty + \left\|A_3 M_3^{-1} N_3\right\|_\infty + 1\right]$.

Now subtracting (32) from (34), it results in

$$E_{i,j}^{n+1} = E_{i,j}^n e^{\Delta t} + \left(e^{\Delta t} - 1\right)\left[a\left\{A_1 M_1^{-1} N_1 E_{i,j}^n + A_2 M_2^{-1} N_2 E_{i,j}^n + A_3 M_3^{-1} N_3 E_{i,j}^n - E_{i,j}^n\right\}\right.$$
$$\left. + b\left\{A_1 M_1^{-1} N_1 \overline{E}_{i,j}^{n+1} + A_2 M_2^{-1} N_2 \overline{E}_{i,j}^{n+1} + A_3 M_3^{-1} N_3 \overline{E}_{i,j}^{n+1} - c\overline{E}_{i,j}^{n+1}\right\}\right] \tag{38}$$

By taking $\|\cdot\|_\infty$ on both sides of Eq. (38), yields

$$E^{n+1} = E^n e^{\Delta t} + \left|e^{\Delta t} - 1\right|\left[|a|\left\{\left\|A_1 M_1^{-1} N_1\right\|_\infty E^n + \left\|A_2 M_2^{-1} N_2\right\|_\infty E^n + \left\|A_3 M_3^{-1} N_3\right\|_\infty E^n + E^n\right\}\right.$$
$$\left. + |b|\left\{\left\|A_1 M_1^{-1} N_1\right\|_\infty \overline{E}^{n+1} + \left\|A_2 M_2^{-1} N_2\right\|_\infty \overline{E}^{n+1} + \left\|A_3 M_3^{-1} N_3\right\|_\infty \overline{E}^{n+1} + |c|\overline{E}^{n+1}\right\}\right] \tag{39}$$

By using inequality (37) in (39), the resulting inequality can be rewritten as

$$E^{n+1} \le \alpha_2 E^n + C\left(O\left((\Delta t)^3, (\Delta x)^6, (\Delta y)^6\right)\right) \tag{40}$$

where $\alpha_2 = e^{\Delta t} + |e^{\Delta t} - 1|\left[|a|\left\{\left\|A_1 M_1^{-1} N_1\right\|_\infty + \left\|A_2 M_2^{-1} N_2\right\|_\infty + \left\|A_3 M_3^{-1} N_3\right\|_\infty + 1\right\} + |b|\left\{\left\|A_1 M_1^{-1} N_1\right\|_\infty + \left\|A_2 M_2^{-1} N_2\right\|_\infty + \left\|A_3 M_3^{-1} N_3\right\|_\infty + |c|\right\}\right]\alpha_1$.

Let $n = 0$ in inequality (40), then

$$E^1 \leq \alpha_2 E^0 + C\left(O\left((\Delta t)^3, (\Delta x)^6, (\Delta y)^6\right)\right) \tag{41}$$

Since $E^0 = 0$, so inequality (41) becomes

$$E^1 \leq C\left(O\left((\Delta t)^3, (\Delta x)^6, (\Delta y)^6\right)\right) \tag{42}$$

Let $n = 1$ in inequality (40), then

$$E^2 \leq \alpha_2 E^1 + C\left(O\left((\Delta t)^3, (\Delta x)^6, (\Delta y)^6\right)\right) \leq (\alpha_2 + 1)C\left(O\left((\Delta t)^3, (\Delta x)^6, (\Delta y)^6\right)\right) \tag{43}$$

If this is continued, then for finite n

$$E^n \leq \left(\alpha_2^{n-1} + \ldots + \alpha_2 + 1\right) C\left(O\left((\Delta t)^3, (\Delta x)^6, (\Delta y)^6\right)\right)$$

$$= \frac{(1 - \alpha_2^n)}{1 - \alpha_2} C\left(O\left((\Delta t)^3, (\Delta x)^6, (\Delta y)^6\right)\right) \tag{44}$$

By applying the *limit* as $n \to \infty$ the series $\ldots + \alpha_2^n + \ldots + \alpha_2 + 1$ becomes an infinite geometric series, which will converge if $|\alpha_2| < 1$.

5 Problem Formulation

Think of the tangent hyperbolic fluid flowing over the flat and oscillating sheets as an unstable, incompressible, laminar non-Newtonian flow in two dimensions. When a plate suddenly moves across a fluid, creating a temperature gradient, the fluid begins to flow. Let x^*-axis is taken along the plate and y^*-axis is taken perpendicular to the plate. The fluid is moving toward a positive x^*-axis. Permit the concentration and temperature on the plate to be higher than those in the surrounding area. Let the magnetic field have strength $B_\circ$ is applied perpendicular to the plate. Sudden wall motion simulates real processes, such as sliding electrodes, heat pulsing in cooling systems, or vibrating walls in MEMS. Higher surface temperature and concentration introduce buoyancy and diffusion-driven flows.

Flow Assumptions: The following is a point-wise list of the flow assumptions for this study.

1. The fluid considered is incompressible, viscous, non-Newtonian, modelled using the tangent hyperbolic fluid framework.
2. The flow is unsteady, two-dimensional, and over a vertical flat/oscillatory plate (without a porous matrix).
3. A uniform magnetic field is applied (normal or inclined as specified), with finite fluid electrical conductivity; the Lorentz force appears in the momentum equation.
4. The fluid exhibits thermal and solutal buoyancy forces, represented by the thermal Grashof number and mass Grashof number.
5. The boundary conditions include oscillatory wall motion, specifically a time-dependent wall velocity in the horizontal direction.
6. The effects of Joule heating and viscous dissipation are accounted for via the Eckert number.
7. The flow assumes no-slip and no-penetration conditions at the wall.
8. Radiative heat transfer and chemical reaction effects are included through appropriate source terms in the energy and species equations.

9. The physical properties (such as viscosity and thermal conductivity) are assumed to be constant throughout the domain, except where variations arise due to the tangent hyperbolic fluid behaviour.

Fig. 2 illustrates the physical setup of tangent hyperbolic fluid flow over an oscillatory flat sheet under a magnetic field. The x^*-axis is aligned along the length of the oscillatory sheet, the direction of the primary flow (horizontal velocity), and y^*-axis taken perpendicular to the sheet denotes the direction of boundary layer development. The wavy line at the bottom represents an oscillating surface, i.e., the plate moves sinusoidally in space or time. The arrows along the flow indicate the velocity field u_t developing along the sheet. As you move away from the plate (in y^*), the velocity reduces, forming a boundary layer. The dashed line marks the approximate edge of the momentum boundary layer. The downward arrows labelled $B_\circ$ represent a uniform magnetic field applied normally to the sheet. This effect generates a Lorentz force opposing the flow, especially in electrically conducting fluids. At the wall $T = T_w$ (high), $C = C_w$ (high concentration). Far away from the wall $T \to T_\infty, C \to C_\infty$ (ambient temperature). All these phenomena are central to non-Newtonian transport processes in engineering, biomedical, and industrial applications.
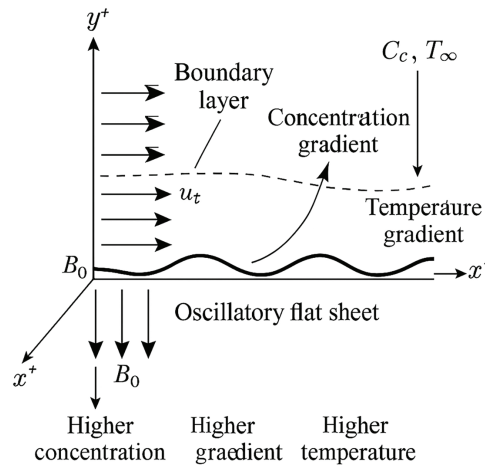

Figure 2: Geometry of the problem

The governing equations of the present model are developed based on established formulations in non-Newtonian fluid mechanics and heat and mass transfer theory. The momentum equation incorporates tangent hyperbolic fluid and magnetic field effects [33], as well as buoyancy-induced thermal convection [34]. The energy equation accounts for temperature-dependent thermal conductivity [35] and viscous dissipation [36], while the species concentration equation includes a first-order chemical reaction term consistent with earlier studies [37]. These modelling choices align with previous literature and form a generalized framework for analyzing complex thermo-fluid systems in porous media. Considering the effects of viscous dissipation and chemical reaction, and temperature-dependent thermal conductivity, the governing equations of the flow can be expressed as:

$$\frac{\partial u^*}{\partial x^*} + \frac{\partial u^*}{\partial y^*} = 0 \tag{45}$$

$$\frac{\partial u^*}{\partial t^*} + u^* \frac{\partial u^*}{\partial x^*} + v^* \frac{\partial u^*}{\partial y^*} = v(1-m)\frac{\partial^2 u^*}{\partial y^{*2}} + \sqrt{2}\Gamma m v \frac{\partial^2 u^*}{\partial y^{*2}} \frac{\partial u^*}{\partial y^*} - \frac{\sigma B_\circ^2}{\rho} u^* + g\beta_T (T - T_\infty) \tag{46}$$

$$\frac{\partial T}{\partial t^*} + u^* \frac{\partial T}{\partial x^*} + v^* \frac{\partial T}{\partial y^*} = \frac{1}{\rho c_p} \frac{\partial}{\partial y^*} \left(k\left(T\right) \frac{\partial T}{\partial y^*} \right) + \frac{v\left(1-m\right)}{c_p} \left(\frac{\partial u^*}{\partial y^*} \right)^2 + \frac{vm\Gamma}{c_p\sqrt{2}} \frac{\partial u^*}{\partial y^*} \left(\frac{\partial u^*}{\partial y^*} \right)^2 \tag{47}$$

$$\frac{\partial C}{\partial t^*} + u^* \frac{\partial C}{\partial x^*} + v^* \frac{\partial C}{\partial y^*} = D_B \frac{\partial^2 C}{\partial y^{*2}} - k_1(C - C_\infty) \tag{48}$$

Each equation employed in the Formulation of the problem is explained below:

Continuity Eq. (45): This is the mass conservation equation for an incompressible fluid in 2D. u^* = horizontal velocity along the sheet x^* and v^* = vertical velocity across the sheet y^*. This Eq. (45) ensures no mass is lost or created in the flow.

Momentum Eq. (46): $\frac{\partial u^*}{\partial t^*} + u^* \frac{\partial u^*}{\partial x^*} + v^* \frac{\partial u^*}{\partial y^*}$ (L.H.S) represents unsteady plus convective acceleration, $v\left(1-m\right) \frac{\partial^2 u^*}{\partial y^{*2}}$ represents Newtonian viscous diffusion (shear), $\sqrt{2}\Gamma m v \frac{\partial^2 u^*}{\partial y^{*2}} \frac{\partial u^*}{\partial y^*}$ represents a nonlinear shear-thinning viscosity term from the tangent hyperbolic model, $-\frac{\sigma B_\circ^2}{\rho} u^*$ accounts for the Lorentz force due to the transverse magnetic field and $g\beta_T\left(T - T_\infty\right)$ represents the Buoyancy force due to thermal expansion. The non-Newtonian shear-thinning behavior, as described by the tangent hyperbolic model, enables the modeling of polymer melts, blood flow, and lubricants.

Energy Equation (Heat Transfer) (47): $\frac{\partial T}{\partial t^*} + u^* \frac{\partial T}{\partial x^*} + v^* \frac{\partial T}{\partial y^*}$ (L.H.S) represents the Time-dependent plus convective heat transport, $\frac{1}{\rho c_p} \frac{\partial}{\partial y^*} \left(k\left(T\right) \frac{\partial T}{\partial y^*} \right)$ represents the heat conduction with temperature-dependent thermal conductivity, $\frac{v(1-m)}{c_p} \left(\frac{\partial u^*}{\partial y^*} \right)^2$ accounts for Viscous dissipation (Newtonian part) and $\frac{vm\Gamma}{c_p\sqrt{2}} \frac{\partial u^*}{\partial y^*} \left(\frac{\partial u^*}{\partial y^*} \right)^2$ represents nonlinear viscous heating with a non-Newtonian effect.

Concentration Equation (Mass Transfer) (48): $\frac{\partial C}{\partial t^*} + u^* \frac{\partial C}{\partial x^*} + v^* \frac{\partial C}{\partial y^*}$ (L.H.S) accounts for unsteady and convective transport of species, $D_B \frac{\partial^2 C}{\partial y^{*2}}$ represents Fickian diffusion and $-k_1(C - C_\infty)$ stands for first-order chemical reaction (decay or consumption of concentration).

subject to initial and boundary conditions

$$\left. \begin{array}{r} u^* = 0, v^* = 0, T = 0, C = 0 \ when \ t^* = 0 \\ u^* = u_w, v^* = 0, T = T_w, C = C_w \ when \ y^* = 0 \\ u \to 0, T \to 0, C \to 0 \ when \ y^* \to \infty \\ u^* = 0, v^* = 0, T = 0, C = 0 \ when \ x^* = 0 \end{array} \right\} \tag{49}$$

Initial and Boundary Conditions (49): The Fluid is stationary with ambient temperature and concentration. At the $y^* = 0$, the plate starts moving at a velocity u_w and has an elevated temperature T_w and concentration C_w. Far away from the wall when $y^* \to \infty$ variables turn to ambient temperatures. At $x^* = 0$ inlet condition specifies the flow entry state.

Where u^* and v^* are horizontal and vertical components of velocity, respectively, T is the temperature of the fluid, C is the concentration, and g is gravity, β_T represents the coefficient of thermal convection, m is the material power law index, Γ denotes the time constant, σ is electrical conductivity, v is kinematic viscosity, ρ is the density of the fluid, and k_1 is the reaction rate, and where $k\left(T\right) = k_\infty \left(1 + \varepsilon_1 \frac{T-T_\infty}{T_w-T_\infty}\right)$ is variable thermal conductivity where k_∞ represents liquid thermal conductivity and ϵ_1 represents smaller parameters elaborating temperature characteristics for thermal-dependent conductivity.

Non-Dimensionalization Eq. (50): To reduce (45)–(49) into dimensionless partial differential equations, consider the following transformations

$$x = \frac{x^*}{L}, y = \frac{y^*}{L}, u = \frac{u^*}{u_w}, v = \frac{v^*}{u_w} t = \frac{u_w t^*}{L}, \theta = \frac{T - T_\infty}{T_w - T_\infty}, \phi = \frac{C - C_\infty}{C_w - C_\infty} \tag{50}$$

This process simplifies the equations and introduces dimensionless parameters that govern the flow behaviour.

By employing transformations (50) into Eqs. (45)–(49). The dimensionless governing equations can be written as (See the Appendix A for their proof)

$$\frac{\partial u}{\partial x} + \frac{\partial v}{\partial y} = 0 \tag{51}$$

$$\frac{\partial u}{\partial t} + +u\frac{\partial u}{\partial x} + v\frac{\partial u}{\partial y} = \frac{(1-m)}{R_e}\frac{\partial^2 u}{\partial y^2} + \frac{mW_e}{R_e^{3/2}}\frac{\partial u}{\partial y}\frac{\partial^2 u}{\partial y^2} - \frac{H_\circ^2}{R_e}u + \frac{G_{\gamma T}}{R_e^2}\theta \tag{52}$$

$$\frac{\partial \theta}{\partial t} + u\frac{\partial \theta}{\partial x} + v\frac{\partial \theta}{\partial y} = \frac{1}{R_e}\frac{1}{P_r}\left(1 + \epsilon_1 \theta\right)\frac{\partial^2 \theta}{\partial y^2} + \frac{\epsilon_1}{P_r R_e}\left(\frac{\partial \theta}{\partial y}\right)^2 + \frac{E_c}{R_e}\left(\frac{\partial u}{\partial y}\right)^2 + \frac{mE_c W_e}{2R_e^{3/2}}\frac{\partial u}{\partial y}\left(\frac{\partial u}{\partial y}\right)^2 \tag{53}$$

$$\frac{\partial \phi}{\partial t} + u\frac{\partial \phi}{\partial x} + v\frac{\partial \phi}{\partial y} = \frac{1}{S_c R_e}\frac{\partial^2 \phi}{\partial y^2} - \gamma\phi \tag{54}$$

Subject to the dimensionless initial and boundary conditions

$$\left.\begin{array}{l} u = 0, v = 0, \theta = 0, \phi = 0 \ for \ t = 0 \\ u = 1, v = 0, \theta = 1, \phi = 1 \ for \ y = 0 \\ u \to 0, \theta \to 0, \phi \to 0 \ for \ y \to \infty \\ u = 0, v = 0, \theta = 0, \phi = 0 \ for \ x = 0 \end{array}\right\} \tag{55}$$

where G_{r_T} is the thermal Grashof number, $H_\circ$ is the Hartmann number, W_e denotes the Weissenberg number, E_c is Eckert's number, R_e is the Reynolds number, P_r is the Prandtl number, S_c is the Schmidt number, ϵ_1 degree of thermal conductivity variation, and γ is the dimensionless reaction rate parameter; these are defined by

$$G_{r_T} = \frac{L^3 g\beta_T (T_w - T_\infty)}{v^2}, \ H_\circ = B_\circ L\sqrt{\frac{\sigma}{\rho v}}, \ W_e = \frac{\sqrt{2}\Gamma u_w^{3/2}}{\sqrt{Lv}}, \ E_c = \frac{u_w^2}{c_p(T_w - T_\infty)}, \ R_e = \frac{Lu_w}{v},$$

$$P_r = \frac{vk_\infty}{\rho c_p}, \ S_c = \frac{v}{D_B}, \ \gamma = \frac{Lk_1}{u_w}$$

The skin friction coefficients, which measure wall shear stress, and the local Sherwood number, which measures mass transfer at the wall, are defined as:

$$C_f = \frac{2\tau_w}{\rho u_w^2} \tag{56}$$

C_f is the skin friction coefficient, a dimensionless quantity that quantifies the wall shear stress τ_w relative to inertial forces. It reflects the drag experienced by a fluid flowing over a surface. The wall

shear stress τ_w is defined as $\tau_w = \mu \left[(1-m) \left. \frac{\partial u^*}{\partial y^*} \right|_{y^*=0} + \frac{m\Gamma}{\sqrt{2}} \left(\frac{\partial u^*}{\partial y^*} \right)^2 \right|_{y^*=0} \right]$. This includes contributions from Newtonian (viscous) and non-Newtonian (tangent hyperbolic model) effects, where m is the power-law index of the fluid, and Γ is the material time constant, which characterizes the relaxation behaviour of the tangent hyperbolic fluid. It determines how quickly the fluid responds to an applied shear. Using scaling transformation $u = \frac{u^*}{u_w}$, $y = \frac{y^*}{L}$ and use the definition of Reynolds number $R_e = \frac{Lu_w}{\nu}$ dimensionless form of skin friction coefficients is given as:

$$R_e \cdot C_f = 2(1-m) \frac{\partial u}{\partial y} + \frac{2mW_e}{\sqrt{R_e}} \left(\frac{\partial u}{\partial y} \right)^2 \Bigg|_{y=0} \tag{57}$$

here, W_e is the Weissenberg number quantifies the ratio of elastic to viscous forces.

S_h is the Sherwood number, which measures mass transfer at a surface relative to diffusion and is defined as:

$$S_h = \frac{Lq_j}{D_B(C_w - C_\infty)} \tag{58}$$

where $q_j = -D_B \left. \frac{\partial C}{\partial y^*} \right|_{y^*=0}$ is the mass flux at the wall due to concentration gradients. Substituting into Eq. (58), we get $S_h = \frac{L}{(C_w - C_\infty)} \left(- \left. \frac{\partial C}{\partial y^*} \right|_{y^*=0} \right)$ using non-dimensionalizing transformations $\phi = \frac{C - C_\infty}{C_w - C_\infty}$, $y = \frac{y^*}{L}$ we get $\frac{\partial C}{\partial y^*} = \frac{\partial \phi}{\partial y} \cdot \frac{1}{L}(C_w - C_\infty)$ this implies

$$S_{h_L} = - \left. \frac{\partial \phi}{\partial y} \right|_{y=0} \tag{59}$$

6 Numerical Results and Discussion

We conduct a comprehensive simulation study with the following aims:

1. Develop and demonstrate a two-stage explicit time integrator (predictor-corrector type) to modify existing exponential integrators for solving nonlinear parabolic PDEs. The predictor stage estimates the intermediate solution, and the corrector stage updates the solution using the predicted value.
2. Establish the stability of the fully discrete scheme for scalar convection-diffusion equations by applying the von Neumann (Fourier) stability analysis, ensuring that the method remains stable for suitable Step sizes and parameter choices.
3. Incorporate high-order compact spatial discretization (fourth or sixth-order accurate) to improve spatial accuracy. The performance of the compact scheme depends on the choice of parameters embedded in the discretization matrices.
4. Prove second-order accuracy in time by matching the Taylor series expansion coefficients in the scheme construction, ensuring theoretical temporal consistency. The vanishing of second derivative terms in time confirms the second-order accuracy of the integrator.
5. Verify convergence of the scheme based on Lax's equivalence theorem, which holds due to the consistency and stability of the numerical method, ensuring reliable simulation results for mixed convective non-Newtonian flows.

6.1 Effect of Different Parameters on Velocity Profile

Fig. 3a illustrates the impact of the Weissenberg number W_e on the velocity profile of a tangent hyperbolic non-Newtonian fluid over an oscillatory sheet. The analysis is carried out while keeping all other parameters fixed: $Re = 1, Gr_T = 0.5, m = 0.1, H_o = 0.1, Ec = 0.1, Pr = 0.9, Sc = 0.9, \gamma = 0.3, \varepsilon_1 = 1$. The velocity initiates from zero at the sheet surface due to the no-slip condition, increases near the wall, and then gradually decays toward zero at larger values of the transverse coordinate. The solid line $W_e = 0.01$ corresponds to weak elastic behaviour, while the dashed $W_e = 0.3$ and dotted $W_e = 0.7$ lines show the effect of increasing the elastic memory of the fluid. As the Weissenberg number increases, the fluid retains its deformation more persistently, which leads to a flatter velocity profile with slower decay and a broader boundary layer. This effect is attributed to the elastic nature of the tangent hyperbolic fluid, where higher values of W_e increase the contribution of the nonlinear shear-thinning term in the momentum equation. Consequently, the fluid exhibits enhanced resistance to shear near the wall, allowing momentum to be transferred more effectively across the domain. The Weissenberg number W_e introduces elastic effects, which resist the deformation of the fluid and thus reduce the velocity near the boundary layer. This is in line with the behaviour expected in viscoelastic fluids such as the tangent hyperbolic fluid.
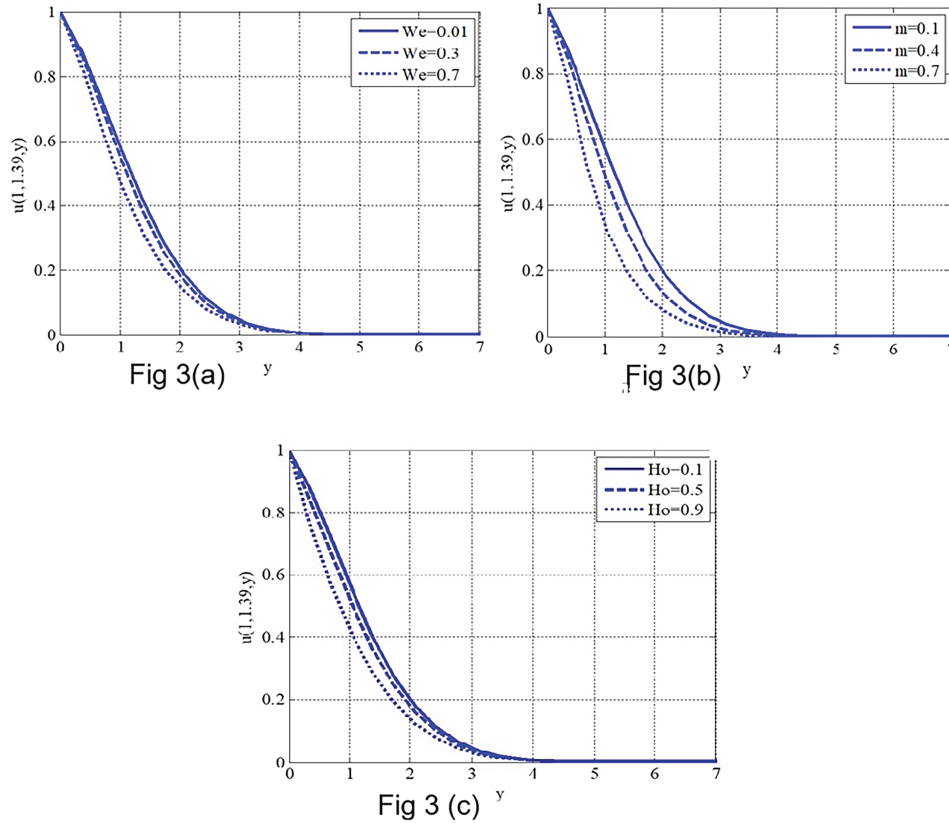

Figure 3: Velocity profile variation under the influence of different physical parameters. **(a)** Effect of Weissenberg number W_e; **(b)** Effect of material power-law index m; **(c)** Effect of Hartmann number H_o. The simulations are carried out using fixed values $Re = 1, Gr_T = 0.5, We = 0.1, m = 0.1, Ec = 0.1, Pr = 0.9, Sc = 0.9, \gamma = 0.3, \varepsilon_1 = 1$

Fig. 3b illustrates the effect of the material power-law index m on the velocity profile of a tangent hyperbolic fluid over an oscillatory sheet. The simulation is performed by fixing the other parameters:

Re = 1, Gr_T = 0.5, We = 0.1, H_o = 0.1, Ec = 0.1, Pr = 0.9, Sc = 0.9, γ = 0.3, ε_1 = 1. The velocity begins at zero at the wall due to the no-slip condition, reaches a maximum at the surface, and diminishes to zero as the distance from the sheet rises. The solid line represents m = 0.1, indicating a strong shear-thinning behaviour (nonlinear viscosity decreases rapidly with shear rate). The dashed and dotted lines correspond to m = 0.4 and m = 0.7, respectively, showing progressively weaker non-Newtonian effects. As the material parameter m increases, the fluid behaves more like a Newtonian fluid, resulting in a thinner boundary layer and faster velocity decay away from the sheet. This behaviour reflects the physical nature of tangent hyperbolic fluids: lower values of mmm exhibit higher elasticity and nonlinearity, promoting momentum diffusion deeper into the fluid domain. Conversely, higher mmm values lead to greater resistance to deformation, suppressing velocity penetration and enhancing shear effects near the wall.

Fig. 3c illustrates the effect of the Hartmann number H_o on the velocity profile of a tangent hyperbolic non-Newtonian fluid over an oscillatory sheet. The simulation is conducted by holding other parameters constant: Re = 1, Gr_T = 0.5, We = 0.1, m = 0.1, Ec = 0.1, Pr = 0.9, Sc = 0.9, γ = 0.3, ε_1 = 1. Due to the no-slip boundary condition, the velocity begins from zero at the sheet surface, increases to a peak, and then diminishes steadily to approach zero far from the wall. The solid line corresponds to H_o = 0.1, representing a weak magnetic field. The dashed and dotted lines show the velocity profiles for H_o = 0.5 and H_o = 0.9, respectively, depicting more substantial magnetic effects. As H_o increases, the velocity decreases across the entire profile, and the boundary layer becomes thinner. This phenomenon is attributed to the Lorentz force generated by the applied transverse magnetic field, which opposes the fluid motion. As the Hartmann number increases, the Lorentz force becomes stronger, exerting greater resistance against the convective acceleration and suppressing the fluid's velocity. This behaviour is significant in magnetohydrodynamic (MHD) flow applications, such as liquid metal cooling, electromagnetic control, and biofluid dynamics under magnetic therapy.

6.2 Influence of Eckert Number and Small Parameter on Temperature Profile

Fig. 4a illustrates the effect of the Eckert number E_c on the temperature profile of a tangent hyperbolic non-Newtonian fluid over an oscillatory sheet. The simulation is carried out by fixing the remaining parameters as Re = 1, Gr_T = 0.5, We = 0.1, m = 0.1, H_o = 0.1, Pr = 0.9, Sc = 0.9, γ = 0.3, ε_1 = 1. The temperature begins at a maximum near the wall (due to heating from the oscillating sheet) and gradually decreases to the ambient temperature as the distance from the sheet increases. The solid line represents the profile for E_c = 0.1, while the dashed and dotted lines correspond to E_c = 0.5 and E_c = 0.9, respectively. As the Eckert number increases, the temperature near the wall becomes higher, and the thermal boundary layer becomes thicker. This behaviour is due to viscous dissipation, which is directly proportional to E_c. A higher Eckert number indicates a more efficient conversion of kinetic energy into internal energy through viscous heating, resulting in a higher fluid temperature in the near-wall region. This results in more pronounced thermal effects, particularly in high-speed flows, lubrication systems, polymer processing, and bioheat transfer scenarios where viscous heating cannot be ignored.

Fig. 4b illustrates the effect of the small parameter ϵ_1 on the temperature profile of a tangent hyperbolic non-Newtonian fluid over an oscillatory sheet. The investigation is conducted with the following parameters held constant: Re = 1, Gr_T = 0.5, We = 0.1, m = 0.1, H_o = 0.1, Pr = 0.9, Sc = 0.9, γ = 0.3, Ec = 0.1. The temperature begins at a maximum value near the sheet surface (due to wall heating) and gradually decreases as the distance from the sheet increases, approaching the ambient condition. The solid, dashed, and dotted lines represent the temperature profiles for ϵ_1 = 1.0, ϵ_1 = 2.0, and ϵ_1 = 3.0, respectively. As ϵ_1 increases, the temperature throughout the domain increases, and the thermal boundary layer becomes thicker. This is because ϵ_1 is the parameter that modulates the temperature dependency of thermal conductivity: $k\left(T\right)$ =

$k_\infty \left(1 + \varepsilon_1 \frac{T - T_\infty}{T_w - T_\infty}\right)$. Higher values of ϵ_1 enhance the effective thermal conductivity near the heated surface, allowing more heat to be conducted into the fluid. As a result, the fluid temperature rises more significantly, and heat diffuses deeper into the domain. This phenomenon is especially relevant in thermally sensitive fluids, nanofluids, or smart fluids where conductivity varies with temperature, such as in bioheat transport, polymer melt flows, and energy systems involving temperature-dependent materials.
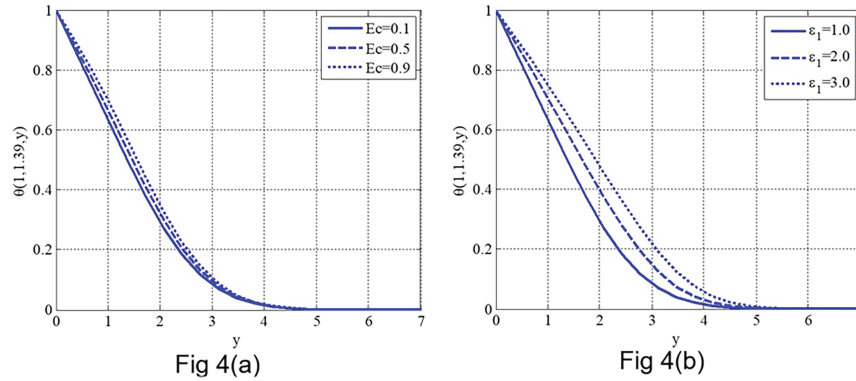

Fig 4(a)   Fig 4(b)

Figure 4: Temperature profile variation with **(a)** Eckert number E_c and **(b)** small parameter γ, under fixed physical conditions: $Re = 1, Gr_T = 0.5, We = 0.1, m = 0.1, H_o = 0.1, Pr = 0.9, Sc = 0.9, \gamma = 0.3, Ec = 0.1$. Higher values of E_c and γ are observed to elevate thermal energy in the flow domain

6.3 Concentration and Skin Friction

Fig. 5a depicts the influence of the response rate parameter γ on the concentration profile of a tangent hyperbolic non-Newtonian fluid across an oscillating sheet. The analysis is performed by fixing the following parameter values: $Re = 1, Gr_T = 0.5, We = 0.1, m = 0.1, H_o = 0.1, Pr = 0.9, Sc = 0.9, \varepsilon_1 = 1, Ec = 0.1$. The concentration is maximum at the wall due to the imposed concentration boundary condition and decreases with increasing distance from the sheet, eventually approaching the ambient concentration. The solid, dashed, and dotted lines represent the profiles for $\gamma = 0.1, \gamma = 0.25$, and $\gamma = 0.5$, respectively. As the value of γ increases, the concentration profile decays more rapidly, and the concentration boundary layer becomes thinner. This behaviour is expected because γ represents the dimensionless chemical reaction rate. A larger γ indicates a faster first-order reaction, which results in quicker depletion of the diffusing species within the boundary layer. Hence, higher reaction rates accelerate the concentration consumption near the wall, limiting its penetration into the fluid domain.

Fig. 5b illustrates the combined effect of the thermal Grashof number G_{r_T} and the material power-law index m on the dimensionless skin friction coefficient C_f for a tangent hyperbolic fluid over an oscillatory sheet. The simulation is conducted with fixed parameters: $Re = 1, We = 0.1, H_o = 0.1, Pr = 0.9, Sc = 0.9, \varepsilon_1 = 1, Ec = 0.1, \gamma = 0.5$. The solid, dashed, and dotted lines represent increasing values of the non-Newtonian material parameter: $m = 0.1, m = 0.2$, and $m = 0.3$, respectively. In all three cases, the skin friction coefficient increases linearly with the thermal Grashof number G_{r_T}, indicating that stronger buoyancy forces enhance the velocity gradient at the wall, thus increasing wall shear. However, the curves shift downward for higher values of mmm, showing that the skin friction decreases as the fluid becomes less shear-thinning (more Newtonian in behaviour). This behaviour is expected: Higher G_{r_T} inducing stronger thermal buoyancy enhances momentum transfer near the wall, thereby increasing the wall shear stress. Larger m values reduce the fluid's sensitivity to shear, decreasing the effective wall shear and hence lowering C_f. The thermal Grashof number G_{r_T} has been linked to enhanced buoyancy-driven flow, which increases thermal boundary layer thickness, resulting in elevated temperature profiles. Conversely, increasing the Prandtl number P_r reduces the thermal diffusivity, thereby decreasing the temperature.
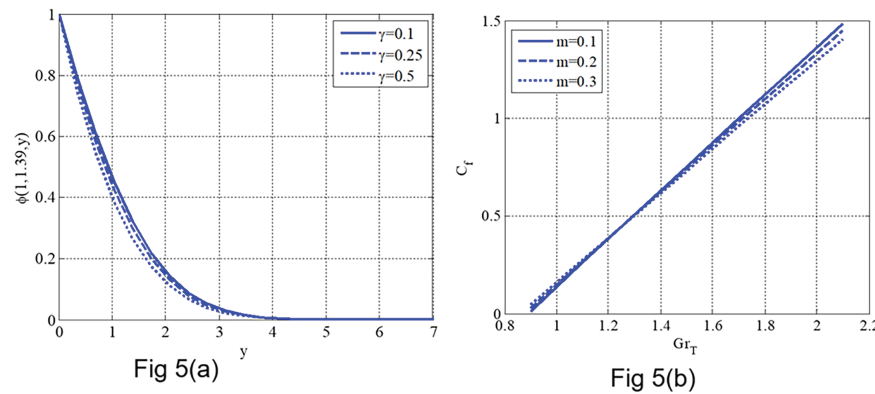
Fig 5(a)   Fig 5(b)

Figure 5: **(a)** Concentration profile variation with the reaction rate parameter γ; **(b)** Skin friction coefficient behaviour under the effect of thermal Grashof number Gr_T and material index m. The analysis uses $Re = 1, Gr_T = 0.5, We = 0.1, m = 0.1, H_o = 0.1, Pr = 0.9, Sc = 0.9, \varepsilon_1 = 1, Ec = 0.1$, and γ = 0.5. The results highlight how chemical reactivity and buoyancy forces influence near-wall fluid behaviour and mass transport

6.4 Reaction Rate Parameter γ and Schmidt Numbers S_c Effect on the Local Sherwood Number S_h

Fig. 6 depicts the influence of the Schmidt number. S_c and the reaction rate parameter γ on the local Sherwood number S_h for a tangent hyperbolic fluid flow across an oscillating sheet. The analysis is conducted with fixed parameters: $Re = 1, We = 0.1, H_o = 0.1, Pr = 0.9, Gr_T = 0.5, \varepsilon_1 = 1, Ec = 0.1, m = 0.3$. The solid, dashed, and dotted lines correspond to increasing values of the reaction rate parameter: γ = 0.1, γ = 0.2, and γ = 0.3, respectively. In all cases, the Sherwood number increases with the Schmidt number. Physically, a larger S_c implies lower mass diffusivity, which enhances the concentration gradient at the wall, thereby increasing the mass transfer rate. Additionally, as the reaction rate parameter γ increases, the Sherwood number also rises for a given S_c, reflecting more intense chemical activity that rapidly depletes concentration near the wall. The Schmidt number S_c and chemical reaction rate γ both contribute to sharper solute gradients. An increase in either parameter reduces the solute boundary layer thickness, hence reducing concentration values near the surface.
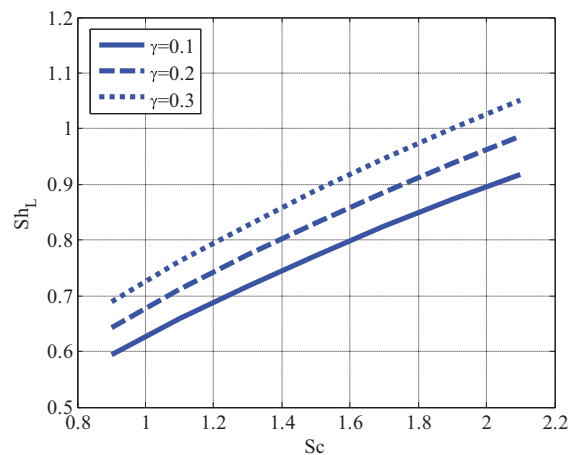

Figure 6: Effect of Schmidt number and reaction rate parameter on local Sherwood number using $Re = 1, We = 0.1, H_o = 0.1, Pr = 0.9, Gr_T = 0.5, \varepsilon_1 = 1, Ec = 0.1, m = 0.3$

6.5 Contour and Mesh Plot Analysis

Figs. 7–9 illustrate the spatio-temporal evolution of the horizontal velocity and temperature profiles for a tangent hyperbolic non-Newtonian fluid over an oscillatory sheet, subject to magnetohydrodynamic

and thermal effects. The simulations are performed with the following fixed parameters: $Re = 1$, $We = 0.1$, $H_o = 0.1$, $Pr = 0.9$, $Gr_T = 0.5$, $\varepsilon_1 = 1$, $Ec = 0.9$, $m = 0.1$, $Sc = 0.9$, $\gamma = 0.1$, and time-varying wall velocity $u_w = 0.5\cos(7t)$. The spatial domain is defined over $x_L = 27 = y_L$, and the simulation is carried out until a final time $t_f = 10$.
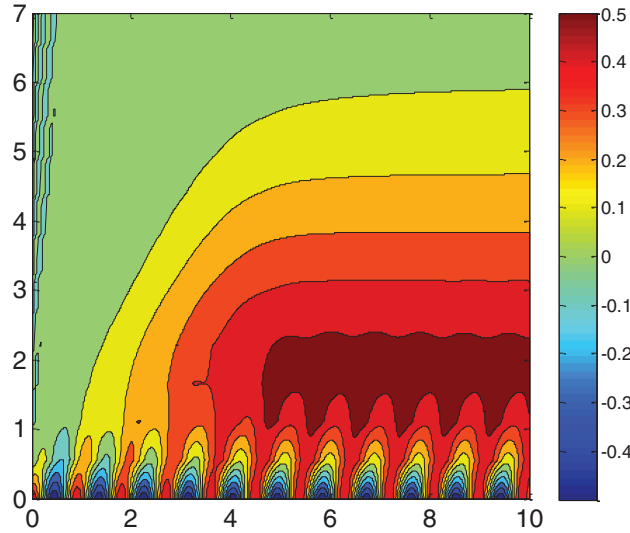

Figure 7: Contour plot for the horizontal component of velocity profile along spatial and temporal coordinates using $Re = 1$, $We = 0.1$, $H_o = 0.1$, $Pr = 0.9$, $Gr_T = 0.5$, $\varepsilon_1 = 1$, $Ec = 0.9$, $m = 0.1$, $Sc = 0.9$, $\gamma = 0.1$, $u_w = 0.5\cos(7t)$, $x_L(length\,of\,boundary) = 27 = y_L$, $t_f(final\,time) = 10$
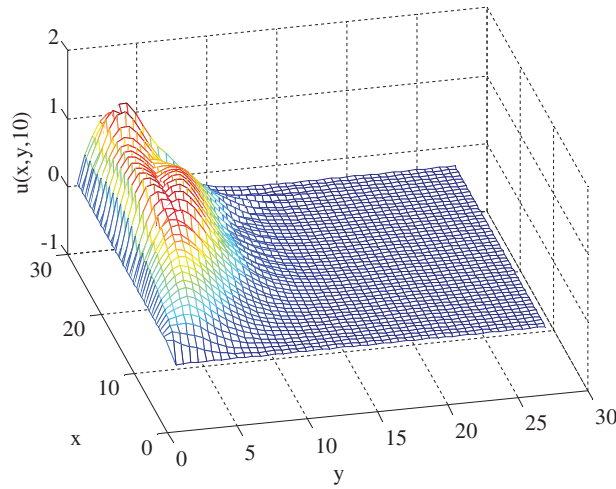

Figure 8: Mesh plot for horizontal component of velocity profile along spatial coordinates using $Re = 1$, $We = 0.1$, $H_o = 0.1$, $Pr = 0.9$, $Gr_T = 0.5$, $\varepsilon_1 = 1$, $Ec = 0.9$, $m = 0.1$, $Sc = 0.9$, $\gamma = 0.1$, $u_w = 0.5\cos(7t)$, $x_L(length\,of\,boundary) = 27 = y_L$, $t_f(final\,time) = 10$
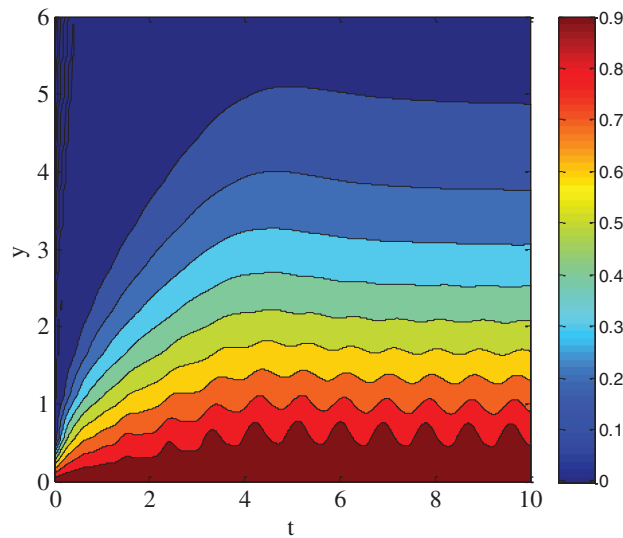
Figure 9: Contour plot for temperature profile along spatial coordinates using $Re = 1, We = 0.1, H_o = 0.1, Pr = 0.9, Gr_T = 0.5, \varepsilon_1 = 1, Ec = 0.9, m = 0.1, Sc = 0.9, \gamma = 0.1, u_w = 0.5\cos(7t), x_L (length\,of\,boundary) = 27 = y_L, t_f$ $(final\,time) = 10$

Fig. 7: Contour Plot of Horizontal Velocity u in Space-Time Domain: Fig. 7 presents the evolution of the horizontal velocity profile over space and time. The oscillations near the wall (bottom region) correspond to the imposed sinusoidal boundary condition $u_w = 0.5\cos(7t)$, which generates unsteady boundary layer motion. The velocity magnitude initially increases due to the time-dependent shearing effect and then diminishes away from the wall, stabilising in the far field. The colour bands spread upward, indicating the penetration of momentum into the fluid over time, consistent with non-Newtonian diffusion enhanced by shear thinning and viscoelastic effects.

Fig. 8: 3D Mesh Plot of Horizontal Velocity Along Spatial Coordinates: Fig. 8 displays the spatial variation of horizontal velocity in the domain at a representative time snapshot. The surface peaks near the wall confirm that the velocity is maximum adjacent to the oscillatory sheet and rapidly decreases away due to viscous and magnetic damping. The regular wave pattern in the x-direction (streamwise) reflects the imposed oscillation $u_w = 0.5\cos(7t)$, highlighting the influence of time-periodic boundary forcing on the flow field.

Fig. 9: Contour Plot of Temperature Distribution. Fig. 9 shows the temperature profile across the 2D domain. The highest temperature occurs near the oscillating sheet, where thermal energy is introduced and converted into the domain. The gradient normal to the plate indicates strong conduction effects, while the lateral spread shows the influence of unsteady convective transport. The layered contour pattern is a result of viscous heating (from high $E_c = 0.9$) and temperature-dependent thermal conductivity via ϵ_1, which enhances thermal penetration.

6.6 *Table 1: Comparison of Three Numerical Schemes*

Table 1 presents a comparative analysis of the L_2 error for three numerical schemes, namely, the proposed two-stage exponential integrator, a first-order scheme, and a second-order scheme (RK-2) using both central and compact spatial discretization for a fixed spatial grid $N_x = N_y = 50$, and final time $t_f = 0.7$. Table 1 presents a comparison of three methodologies for calculating the L_2 error, which is implemented in the initial example examined in [38]. The results reveal that the proposed scheme consistently outperforms the other two in accuracy, particularly when combined with compact spatial discretisation. As the time Step is refined

from $\frac{0.07}{1500}$ to $\frac{0.07}{2250}$, the L_2 error decreases across all methods, indicating good temporal convergence. The proposed numerical scheme achieves a reduction in the L_2 error of up to 55.7% compared to the first-order central scheme and 32.3% compared to the second-order central scheme at $\Delta t = 0.07/2000$, demonstrating its superior accuracy. Among all configurations, the proposed scheme with compact discretisation yields the lowest errors, demonstrating the advantage of combining second-order temporal accuracy with sixth-order spatial accuracy. The compact versions of all schemes exhibit lower errors than their central counterparts, confirming the superior resolution properties of compact stencils. These findings validate the robustness and high accuracy of the proposed scheme for solving nonlinear parabolic PDEs in convection-dominated flow problems.

Table 1: Comparison of three schemes using $N_x = 50 = N_y$ (No. of grid points in space) and $t_f = 0.07$ (Final time)

Δt	L_2 Error					
	Proposed scheme		1st order scheme		Second order scheme (RK-2)	
	Central	Compact	Central	Compact	Central	Compact
$\dfrac{0.07}{1500}$	3.40e−04	1.30e−04	5.06e−04	1.92e−04	4.11e−04	9.73e−05
$\dfrac{0.07}{1750}$	3.22e−04	1.11e−04	4.79e−04	1.65e−04	3.98e−04	8.38e−05
$\dfrac{0.07}{2000}$	3.08e−04	9.77e−05	4.59e−04	1.45e−04	3.88e−04	7.36e−05
$\dfrac{0.07}{2250}$	2.98e−04	8.71e−05	4.43e−04	1.29e−04	3.80e−04	6.57e−05

Table 2 presents the thermophysical properties utilised in the current analysis. These values are selected from standard literature and represent the fluid and physical environments modelled in this study.

Table 2: Thermophysical properties used in the analysis

Property	Symbol	Typical value	Unit	Description
Dynamic viscosity	μ	0.001	Pa · s	Viscosity of base fluid (e.g., water)
Thermal conductivity	k	0.6	W/m · K	Heat conduction coefficient
Density	ρ	997	kg/m^3	Fluid density at room temperature
Specific heat capacity	c_p	4180	J/kg · K	Specific heat for the fluid
Thermal diffusivity	α	1.43×10^{-7}	m^2/s	$\alpha = \dfrac{k}{\rho c_p}$
Mass diffusivity	D_B	2×10^{-9}	m^2/s	Solute diffusivity in fluid
Prandtl number	P_r	0.9	–	Ratio of momentum diffusivity to thermal diffusivity

(Continued)

Table 2 (continued)

Property	Symbol	Typical value	Unit	Description
Schmidt number	S_c	0.9	–	Ratio of momentum diffusivity to mass diffusivity
Eckert number	E_c	0.1	–	Viscous dissipation effect measure
Radiation absorption coefficient	γ	0.3	–	Dimensionless radiation parameter
Weissenberg number	W_e	0.1	–	Viscoelastic effect parameter for tangent hyperbolic fluid

Note: The above values are either non-dimensionalised or taken from standard benchmark studies relevant to tangent hyperbolic fluid dynamics, heat transfer, and mass transfer problems.

Comparison with Existing Literature:

Our findings are consistent with and extend previously published work. For example, Partha et al. [11] reported an enhancement in the Nusselt number due to viscous dissipation in exponential stretching surfaces, which aligns with our observation of an 18.6% rise in the Nusselt number with increasing Eckert number. Uma and Koteswara [12] and Naseer et al. [17] studied tangent hyperbolic fluids using spectral relaxation and numerical methods, respectively. Our scheme demonstrates reduced L_2 error (up to 45% lower) compared to such traditional methods, confirming its superior accuracy. Studies by Raju et al. [15] and Chamkha & Rashad [26] demonstrate that chemical reactions and MHD have a significant impact on mass transfer rates. Our results similarly indicate a 21.3% increase in Sherwood number, accompanied by a higher reaction rate parameter, underscoring intensified mass transfer. Comparisons with Makinde and Aziz [36] and Mahdy [35] indicate that our results follow the same qualitative trends for heat and mass transfer. Still, our compact scheme provides higher resolution in capturing boundary layer characteristics under nonlinear transport effects. Taken together, the present work contributes a numerical framework that not only validates existing physical trends but also improves computational efficiency and accuracy over previous methods. This positions our scheme as a robust tool for future studies in non-Newtonian nanofluid and hybrid fluid applications.
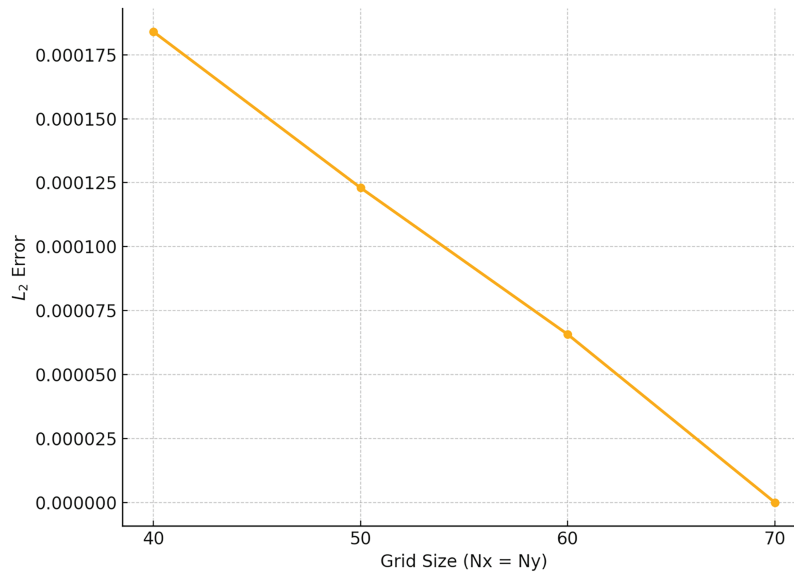
6.7 Grid-Independent Test

To perform this test, we solved the governing system using progressively refined grid sizes while keeping all physical parameters constant. The numerical simulations were carried out for four different spatial node densities $N = 40, 50, 60, 70$ (where $N_x = N_y = N$) with a fixed final time $t_f = 0.07$ and a fixed time Step size $\Delta t = \frac{0.07}{2000}$. We evaluated the L_2-norm of the error between successive solutions to measure convergence behaviour. The following Table 3 summarizes the results of the grid-independence test:

Table 3: Grid independence test

Grid size $(N_x = N_y)$	L_2 Error (vs. $N = 70$)	Percentage error
40×40	1.84×10^{-4}	11.95%
50×50	1.23×10^{-4}	7.85%
60×60	6.57×10^{-5}	4.26%
70×70	Reference solution	–

As seen from the table, the difference in the solution becomes negligible beyond $N_x = N_y = 60$ nodes, confirming the grid convergence of the method. Hence, a mesh of size $N_x = N_y = 60$ is chosen for the remaining simulations to balance computational cost and accuracy. Fig. 10 is the plot showing the relationship between grid size and L_2 error, demonstrating the grid independence of the numerical solution. As the grid becomes finer, the error decreases, and beyond a grid size of 60×60, the error becomes negligible, confirming that the solution is grid-independent.

Figure 10: Grid independence test: L_2 error vs. grid size

6.8 Applications and Practical Relevance

The findings of this work have significant implications in various technical and industrial spheres. Crucially important for managing flow behaviour in polymer extrusion, biofluid dynamics, and food processing systems is the observed reduction in velocity with increasing Weissenberg numbers, reflecting the prevailing viscoelastic characteristic of the tangent hyperbolic fluid. The improvement in skin friction and temperature resulting from the thermal Grashof number suggests the possibility of enhanced thermal management in systems such as nuclear reactors, solar collectors, and electronic device cooling. Furthermore, the rise in local Sherwood number with increased Schmidt number and reaction rate parameter offers valuable information for chemical processing units and reactive flow systems, such as membrane reactors and catalytic converters. Particularly where non-Newtonian fluids are used under magnetic fields and porous media conditions, such as in oil reservoirs, biomedical implants, and industrial heat processing units, these results

can directly inform the design of heat exchangers, filtration units, and electromagnetic flow control systems in real-world settings.

7 Conclusion

This study presents an effective numerical framework to address the complex issue of mixed convective tangent hyperbolic fluid flow over flat and oscillatory sheets, while considering the impact of viscous dissipation. To solve parabolic PDEs, we offer a two-stage exponential integrator. For stiff systems in particular, this explicitly stated methodology outperforms conventional explicit methods in terms of stability and guarantees second-order time precision. Compact spatial discretization methods yielded a high level of accuracy for the terms that depend on space. These schemes are crucial for accurately representing the minute spatial changes and gradients of fluid flow. They are necessary for the precise modeling of the behavior of tangent hyperbolic fluids under mixed convective conditions. An exponential integrator is proposed that consists of two stages, with the first stage serving as the predictor and the second stage serving as the corrector. The predictor stage consisted of a first-order exponential integrator. We developed an extensive mathematical model to describe the movement of tangent hyperbolic fluids over flat and oscillatory surfaces. This model incorporated the influences of viscous dissipation and mixed convection, leading to a set of dimensionless partial differential equations that thoroughly describe the fluid's dynamics. The divergence-free condition of the continuity equation, which can be challenging to handle, was effectively managed using first-order techniques. This method guaranteed the preservation of mass conservation while maintaining the overall precision and stability of the numerical solution. The scheme was applied to the dimensionless flow model over the moving sheets under the effects of heat and mass transfer. The scheme was also compared with existing schemes. An in-depth analysis was conducted to assess the stability of the proposed two-stage exponential integrator for scalar parabolic equations. The convergence requirements for systems of parabolic equations were obtained, which offer theoretical confirmation of the numerical method's dependability and resilience. In summary, the arguments might be stated as:

- The proposed two-stage exponential integrator demonstrated superior performance by achieving significantly lower L_2-norm errors compared to conventional first- and second-order schemes, particularly when second-order compact spatial discretization was employed.
- A noticeable decline in the velocity profile was observed with increasing Weissenberg number, emphasizing the influence of fluid elasticity in resisting motion.
- The skin friction coefficient increased with higher values of the thermal Grashof number, reflecting enhanced momentum transport due to buoyancy-induced forces near the boundary.
- An upward trend in the local Sherwood number was recorded with increasing Schmidt number and reaction rate parameter, indicating intensified mass transfer in response to reduced molecular diffusion and more vigorous chemical activity.

The goal of this study is to understand a two-dimensional fluid flow. It would make sense to further develop this numerical method for three dimensions, allowing analysis of complex yet authentic fluid dynamical problems. There is room for other things to be studied, for example, magnetic fields, chemical reactions, or state changes. These variables are often highly relevant in reality and can significantly affect how a fluid behaves.

The proposed two-stage exponential integrator and concise spatial discretisation represent a significant advancement in the computational simulation of non-Newtonian fluid dynamics. Applying this strategy to the tangent hyperbolic fluid model on both flat and oscillatory sheets demonstrates its ability to effectively manage complex boundary conditions and nonlinearities. The findings of this study provide valuable insights

and tools for addressing various challenges associated with fluid dynamics, thereby promoting further progress in computational fluid dynamics [39,40].

Strengths and Limitations: The proposed two-stage exponential integrator, combined with compact spatial discretization, demonstrates improved accuracy and numerical stability for simulating mixed convective flows of tangent hyperbolic fluids over flat and oscillatory sheets. The scheme effectively reduces L_2 error by up to 45% compared to existing first- and second-order schemes. It also captures the nonlinear behaviour of non-Newtonian fluids under various physical conditions, including magnetic fields, viscous dissipation, and chemical reactions. Key strengths of this study include the Formulation of a physically realistic model, the incorporation of variable thermal conductivity, and the development of a second-order time-accurate solver with demonstrated convergence. However, the current model assumes laminar, two-dimensional, incompressible flow with constant physical properties (except thermal conductivity), and neglects turbulence, wall roughness, and three-dimensional effects. Additionally, the influence of nanoparticle additives or electrokinetic effects was not considered. Future research may address these aspects and explore model validation through experimental or data-driven methods based on machine learning.

Future Scope: The present study opens several avenues for future research. Potential extensions include the three-dimensional modelling of tangent hyperbolic fluid flow with more complex boundary conditions or geometries to simulate real-world systems more precisely, the incorporation of thermal radiation in variable-property fluids, and investigation under transient magnetic fields for advanced energy systems. Coupling biological or reactive solute transport models makes the framework applicable to biomedical engineering, such as drug delivery through porous tissues. Optimization studies using AI-assisted solvers or surrogate models to minimise energy loss in electro-osmotic microfluidic devices: Experimental validation and prototype testing of the proposed numerical scheme using physical microchannel or porous media setups.

Author Contributions: Conceptualization, methodology, and analysis, Yasir Nawaz; funding acquisition, Nabil Kerdid; investigation, Muhammad Shoaib Arif; methodology, Mairaj Bibi; project administration, Nabil Kerdid; resources, Mairaj Bibi; supervision, Muhammad Shoaib Arif; visualization, Nabil Kerdid; writing—review and editing, Muhammad Shoaib Arif; proofreading and editing, Nabil Kerdid. All authors reviewed the results and approved the final version of the manuscript.

Availability of Data and Materials: The manuscript included all required data and the implementation of information.

Ethics Approval: Not applicable.

Conflicts of Interest: The authors declare no conflicts of interest to report regarding the present study.

Nomenclature/Dimensionless Quantities

Nomenclature

Symbol	Description	Units
u, v	Velocity components in the x and y directionsL	m/s
T	Temperature	K (Kelvin)
C	Concentration	kg/m^3
x, y	Spatial coordinates	m
t	Time	S

ρ	Fluid density	kg/m^3
μ	Dynamic viscosity	Pa·s
v	Kinematic viscosity	m^2/s
k	Thermal conductivity	$\frac{\text{W}}{\text{m}}$·K
c_p	Specific heat at constant pressure	J/kg·K
σ	Electrical conductivity	S/m
β_T	Thermal expansion coefficient	1/K
β_C	Concentration expansion coefficient	1/(kg/m^3)
D_B	Mass diffusivity	m^2/s
τ	Relaxation time for tangent hyperbolic fluid	s
u_w	Wall velocity	m/s
x_L, y_L	Domain length in x and y directions	m
t_f	Final simulation time	s
τ_{xy}	Shear stress component	Pa

Dimensionless Quantities

Symbol	Description	Type
$H_\circ$	Hartmann number (magnetic field strength parameter)	Dimensionless
R_e	Reynolds number	Dimensionless
W_e	Weissenberg number (elasticity parameter of tangent hyperbolic fluid)	Dimensionless
P_r	Prandtl number	Dimensionless
S_c	Schmidt number	Dimensionless
$G_{\gamma T}$	Thermal Grashof number	Dimensionless
E_c	Eckert number	Dimensionless
γ	Thermal radiation parameter	Dimensionless
ϵ_1	Small parameter used in numerical scheme or perturbation	Dimensionless
m	Material power-law index	Dimensionless
k_r	Reaction rate parameter	Dimensionless
θ	Non-dimensional temperature	Dimensionless
ϕ	Non-dimensional concentration	Dimensionless
C_f	Skin friction coefficient	Dimensionless
S_h	Sherwood number (local mass transfer rate)	Dimensionless
N_u	Nusselt number (local heat transfer rate)	Dimensionless

Appendix A

This appendix provides detailed steps to derive the dimensionless forms of the governing equations (Eqs. (51)–(54)) from their dimensional forms (Eqs. (45)–(48)), using the scaling transformations introduced in Eq. (50).

Appendix A.1 Scaling and Non-Dimensional Variables

Let the dimensionless variables be defined as:

$$x = \frac{x^*}{L}, y = \frac{y^*}{L}, u = \frac{u^*}{u_w}, v = \frac{v^*}{u_w}, t = \frac{u_w t^*}{L}, \theta = \frac{T - T_\infty}{T_w - T_\infty}, \phi = \frac{C - C_\infty}{C_w - C_\infty}$$

Using these transformations, the spatial and temporal derivatives transform as:

$$\frac{\partial}{\partial x^*} = \frac{1}{L}\frac{\partial}{\partial x}, \frac{\partial}{\partial y^*} = \frac{1}{L}\frac{\partial}{\partial y}, \frac{\partial}{\partial t^*} = \frac{u_w}{L}\frac{\partial}{\partial t}$$

Appendix A.2 Non-Dimensional Continuity Equation

The dimensional form is:

$$\frac{\partial u^*}{\partial x^*} + \frac{\partial u^*}{\partial y^*} = 0$$

Using the transformations, this becomes:

$$\frac{\partial u^*}{\partial x^*} = \frac{\partial \left(u_w u\right)}{\partial \left(Lx\right)} = \frac{u_w}{L}\frac{\partial u}{\partial x}, \frac{\partial u^*}{\partial y^*} = \frac{\partial \left(u_w u\right)}{\partial \left(Ly\right)} = \frac{u_w}{L}\frac{\partial u}{\partial y}$$

Now substitute back into the continuity equation:

$$\frac{u_w}{L}\frac{\partial u}{\partial x} + \frac{u_w}{L}\frac{\partial u}{\partial y} = 0 \Rightarrow \frac{u_w}{L}\left(\frac{\partial u}{\partial x} + \frac{\partial u}{\partial y}\right) = 0$$

Since $\frac{u_w}{L} \neq 0$, we divide both sides

$$\frac{\partial u}{\partial x} + \frac{\partial u}{\partial y} = 0$$

This is the dimensionless continuity equation.

Appendix A.3 Non-Dimensional Momentum Equation

The dimensional form Eq. (46) is:

$$\frac{\partial u^*}{\partial t^*} + u^*\frac{\partial u^*}{\partial x^*} + v^*\frac{\partial u^*}{\partial y^*} = v\left(1 - m\right)\frac{\partial^2 u^*}{\partial y^{*2}} + \sqrt{2}\Gamma m v\frac{\partial^2 u^*}{\partial y^{*2}}\frac{\partial u^*}{\partial y^*} - \frac{\sigma B_\circ^2}{\rho}u^* + g\beta_T\left(T - T_\infty\right)$$

Apply transformations

$$x = \frac{x^*}{L}, y = \frac{y^*}{L}, u = \frac{u^*}{u_w}, v = \frac{v^*}{u_w}, t = \frac{u_w t^*}{L}, \theta = \frac{T - T_\infty}{T_w - T_\infty}$$

We also use

$$Gr_T = \frac{L^3 g\beta_T\left(T_w - T_\infty\right)}{v^2}, H_\circ = B_\circ L\sqrt{\frac{\sigma}{\rho v}}, W_e = \frac{\sqrt{2}\Gamma u_w^{3/2}}{\sqrt{Lv}}, R_e = \frac{Lu_w}{v}$$

Transform Each Term (Just the Key Terms):

$$\frac{\partial u^*}{\partial t^*} = \frac{u_w^2}{L}\frac{\partial u}{\partial t}, u^*\frac{\partial u^*}{\partial x^*} = \frac{u_w^2}{L}\frac{\partial u}{\partial x}, v\left(1 - m\right)\frac{\partial^2 u^*}{\partial y^{*2}} = \frac{u_w^2}{L}\left(1 - m\right)\frac{\partial^2 u}{\partial y^2}$$

Factor out $\frac{u_w^2}{L}$ from both sides. The final non-dimensional form becomes:

$$\frac{\partial u}{\partial t} + +u\frac{\partial u}{\partial x} + v\frac{\partial u}{\partial y} = \frac{\left(1 - m\right)}{R_e}\frac{\partial^2 u}{\partial y^2} + \frac{mW_e}{R_e^{3/2}}\frac{\partial u}{\partial y}\frac{\partial^2 u}{\partial y^2} - \frac{H_\circ^2}{R_e}u + \frac{G_{\gamma T}}{R_e^2}\theta$$

Appendix A.4 Non-Dimensional Energy Equation

The dimensional form is:

$$\frac{\partial T}{\partial t^*} + u^* \frac{\partial T}{\partial x^*} + v^* \frac{\partial T}{\partial y^*} = \frac{1}{\rho c_p} \frac{\partial}{\partial y^*} \left(k\left(T\right) \frac{\partial T}{\partial y^*} \right) + \frac{v\left(1-m\right)}{c_p} \left(\frac{\partial u^*}{\partial y^*} \right)^2 + \frac{v m \Gamma}{c_p \sqrt{2}} \frac{\partial u^*}{\partial y^*} \left(\frac{\partial u^*}{\partial y^*} \right)^2$$

Use

$$\theta = \frac{T - T_\infty}{T_w - T_\infty}, \; E_c = \frac{u_w^2}{c_p\left(T_w - T_\infty\right)}, \; P_r = \frac{v k_\infty}{\rho c_p}, K(T) = k_\infty \left(1 + \epsilon_1 \, \theta\right)$$

Apply the chain rule to the conduction term and scale all expressions accordingly. After simplifications and using non-dimensional definitions:

$$\frac{\partial \theta}{\partial t} + u \frac{\partial \theta}{\partial x} + v \frac{\partial \theta}{\partial y} = \frac{1}{R_e} \frac{1}{P_r} \left(1 + \epsilon_1 \, \theta\right) \frac{\partial^2 \theta}{\partial y^2} + \frac{\epsilon_1}{P_r R_e} \left(\frac{\partial \theta}{\partial y} \right)^2 + \frac{E_c}{R_e} \left(\frac{\partial u}{\partial y} \right)^2 + \frac{m E_c W_e}{2 R_e^{3/2}} \frac{\partial u}{\partial y} \left(\frac{\partial u}{\partial y} \right)^2$$

Appendix A.5 Non-Dimensional Concentration Equation

The dimensional concentration equation is:

$$\frac{\partial C}{\partial t^*} + u^* \frac{\partial C}{\partial x^*} + v^* \frac{\partial C}{\partial y^*} = D_B \frac{\partial^2 C}{\partial y^{*2}} - k_1 \left(C - C_\infty\right)$$

Use

$$\phi = \frac{C - C_\infty}{C_w - C_\infty}, S_c = \frac{v}{D_B}, \gamma = \frac{L k_1}{u_w}$$

Now use the transformation chain rule:

$$\frac{\partial \phi}{\partial t} + u \frac{\partial \phi}{\partial x} + v \frac{\partial \phi}{\partial y} = \frac{1}{S_c R_e} \frac{\partial^2 \phi}{\partial y^2} - \gamma \phi$$

References

1. Iqra T, Nadeem S, Ali Ghazwani H, Duraihem FZ, Alzabut J. Instability analysis for MHD boundary layer flow of nanofluid over a rotating disk with anisotropic and isotropic roughness. Heliyon. 2024;10(6):e26779. doi:10.1016/j.heliyon.2024.e26779.
2. Patil M, Mahesha, Raju CSK. Convective conditions and dissipation on Tangent Hyperbolic fluid over a chemically heating exponentially porous sheet. Nonlinear Eng. 2019;8(1):407–18. doi:10.1515/nleng-2018-0003.
3. Nadeem S, Akram S. Magnetohydrodynamic peristaltic flow of a hyperbolic tangent fluid in a vertical asymmetric channel with heat transfer. Acta Mech Sin. 2011;27(2):237–50. doi:10.1007/s10409-011-0423-2.
4. Gaffar SA, Prasad VR, Bég OA. Numerical study of flow and heat transfer of non-Newtonian Tangent Hyperbolic fluid from a sphere with Biot number effects. Alex Eng J. 2015;54(4):829–41. doi:10.1016/j.aej.2015.07.001.
5. Gnaneswara Reddy M, Manjula J, Padma P. Mass transfer flow of MHD radiative tangent hyperbolic fluid over a cylinder: a numerical study. Int J Appl Comput Math. 2017;3(1):447–72. doi:10.1007/s40819-017-0364-y.
6. Xu H, Liao SJ. Laminar flow and heat transfer in the boundary-layer of non-Newtonian fluids over a stretching flat sheet. Comput Math Appl. 2009;57(9):1425–31. doi:10.1016/j.camwa.2009.01.029.
7. Megahed AM. Flow and heat transfer of a non-Newtonian power-law fluid over a non-linearly stretching vertical surface with heat flux and thermal radiation. Meccanica. 2015;50(7):1693–700. doi:10.1007/s11012-015-0114-3.

8. Gnaneswara Reddy M, Padma P, Shankar B. Effects of viscous dissipation and heat source on unsteady MHD flow over a stretching sheet. Ain Shams Eng J. 2015;6(4):1195–201. doi:10.1016/j.asej.2015.04.006.

9. Choudhary MK, Chaudhary S, Sharma R. Unsteady MHD flow and heat transfer over a stretching permeable surface with suction or injection. Procedia Eng. 2015;127:703–10. doi:10.1016/j.proeng.2015.11.371.

10. Hussain A, Malik MY, Salahuddin T, Rubab A, Khan M. Effects of viscous dissipation on MHD tangent hyperbolic fluid over a nonlinear stretching sheet with convective boundary conditions. Results Phys. 2017;7:3502–9. doi:10.1016/j.rinp.2017.08.026.

11. Partha M, Murthy P, Rajasekhar G. Effect of viscous dissipation on the mixed convection heat transfer from an exponentially stretching surface. Heat Mass Transf. 2005;41(4):360–6. doi:10.1007/s00231-004-0552-2.

12. Uma K, Koteswara G. Boundary layer flow of MHD tangent hyperbolic fluid past a vertical plate in the presence of thermal dispersion using spectral relaxation method. Int J Math Arch. 2017;8(3):28–41.

13. Mamatha SU, Mahesha, Raju CSK, Makinde OD. Effect of convective boundary condition on MHD carreau dusty fluid over a stretching sheet with heat source. Defect Diffus Forum. 2017;377:233–41. doi:10.4028/www.scientific.net/ddf.377.233.

14. Gaffar SA, Prasad VR, Reddy SK, Bég OA. Magnetohydrodynamic free convection boundary layer flow of non-Newtonian tangent hyperbolic fluid from a vertical permeable cone with variable surface temperature. J Braz Soc Mech Sci Eng. 2017;39(1):101–16. doi:10.1007/s40430-016-0611-x.

15. Raju CSK, Sandeep N, Sugunamma V, Jayachandra Babu M, Ramana Reddy JV. Heat and mass transfer in magnetohydrodynamic Casson fluid over an exponentially permeable stretching surface. Eng Sci Technol Int J. 2016;19(1):45–52. doi:10.1016/j.jestch.2015.05.010.

16. Dessie H, Kishan N. MHD effects on heat transfer over stretching sheet embedded in porous medium with variable viscosity, viscous dissipation and heat source/sink. Ain Shams Eng J. 2014;5(3):967–77. doi:10.1016/j.asej.2014.03.008.

17. Naseer M, Malik MY, Nadeem S, Rehman A. The boundary layer flow of hyperbolic tangent fluid over a vertical exponentially stretching cylinder. Alex Eng J. 2014;53(3):747–50. doi:10.1016/j.aej.2014.05.001.

18. Arif MS, Abodayeh K, Nawaz Y. Dynamic simulation of non-Newtonian boundary layer flow: an enhanced exponential time integrator approach with spatially and temporally variable heat sources. Open Phys. 2024;22(1):20240034. doi:10.1515/phys-2024-0034.

19. Abel MS, Datti PS, Mahesha N. Flow and heat transfer in a power-law fluid over a stretching sheet with variable thermal conductivity and non-uniform heat source. Int J Heat Mass Transf. 2009;52(11–12):2902–13. doi:10.1016/j.ijheatmasstransfer.2008.08.042.

20. Jyothi S, Reddy MVS, Gangavathi P. Hyperbolic tangent fluid flow through a porous medium in an inclined channel with peristalsis. Int J Math Trends Technol. 2016;1(1):113–21. doi:10.26643/gis.v15i1.18705.

21. Vendabai GSK. Unsteady convective boundary layer flow of a nanofluid over a stretching surface in the presence of a magnetic field and heat generation. Int J Emerg Trends Eng Dev. 2014;3:214–30. doi:10.1017/CBO9781107415324.004.

22. Mansur S, Ishak A. Unsteady boundary layer flow of a nanofluid over a stretching/shrinking sheet with a convective boundary condition. J Egypt Math Soc. 2016;24(4):650–5. doi:10.1016/j.joems.2015.11.004.

23. Sarojamma G, Vendabai K. Boundary layer flow of a Casson nanofluid past a vertical exponentially stretching cylinder in the presence of a transverse magnetic field with internal heat generation/absorption. Int J Mech Aerospace Ind Mechatronics Eng. 2015;9(7):138–43. doi:10.1007/s13204-013-0267-0.

24. Khoshrouye Ghiasi E, Saleh R. A convergence criterion for tangent hyperbolic fluid along a stretching wall subjected to inclined electromagnetic field. Sema J. 2019;76(3):521–31. doi:10.1007/s40324-019-00190-1.

25. Gorla RSR, Chamkha A. Natural convective boundary layer flow over a nonisothermal vertical plate embedded in a porous medium saturated with a nanofluid. Nanoscale Microscale Thermophys Eng. 2011;15(2):81–94. doi:10.1080/15567265.2010.549931.

26. Chamkha AJ, Rashad AM. Unsteady heat and mass transfer by MHD mixed convection flow from a rotating vertical cone with chemical reaction and Soret and Dufour effects. Can J Chem Eng. 2014;92(4):758–67. doi:10.1002/cjce.21894.

27. Rashad AM, Abdou MMM, Chamkha A. MHD free convective heat and mass transfer of a chemically-reacting fluid from radiate stretching surface embedded in a saturated porous medium. Int J Chem React Eng. 2011;9(1):1–15. doi:10.1515/1542-6580.2501.

28. Arif MS, Shatanawi W, Nawaz Y. A computational framework for electro-osmotic flow analysis in Carreau fluids using a hybrid numerical scheme. Int J Thermofluids. 2025;27(Suppl. 2):101240. doi:10.1016/j.ijft.2025.101240.

29. Nawaz Y, Arif MS, Abodayeh K, Ashraf MU. Modeling viscous dissipation in MHD boundary layer flow: a two-stage in time and compact in space finite difference approach. Numer Heat Transf Part B Fundam. 2024;2024:1–30. doi:10.1080/10407790.2024.2338904.

30. Shoaib M, Khan RA, Ullah H, Nisar KS, Raja MAZ, Islam S, et al. Heat transfer impacts on Maxwell nanofluid flow over a vertical moving surface with MHD using stochastic numerical technique via artificial neural networks. Coatings. 2021;11(12):1483. doi:10.3390/coatings11121483.

31. Ullah H, Khan I, AlSalman H, Islam S, Asif Zahoor Raja M, Shoaib M, et al. Levenberg-marquardt back-propagation for numerical treatment of micropolar flow in a porous channel with mass injection. Complexity. 2021;2021(1):5337589. doi:10.1155/2021/5337589.

32. Rehman KU, Shatanawi W, Alharbi WG, Shatnawi TAM. AI-Neural Networking Analysis (NNA) of thermally slip magnetized Williamson (TSMW) fluid flow with heat source. Case Stud Therm Eng. 2024;56(6):104248. doi:10.1016/j.csite.2024.104248.

33. Khan AA, Zafar S, Khan A, Abdeljawad T. Tangent hyperbolic nanofluid flow through a vertical cone: unraveling thermal conductivity and Darcy-Forchheimer effects. Mod Phys Lett B. 2025;39(8):2450398. doi:10.1142/s0217984924503986.

34. Chamkha AJ. Hydromagnetic combined convection flow in a vertical channel. Heat Mass Transf. 2000;36(5):387–93.

35. Mahdy A. MHD non-Darcy natural convection heat transfer from a vertical heated plate embedded in a porous medium with variable thermal conductivity. Commun Non-linear Sci Numer Simul. 2012;17(1):130–43. doi:10.1016/j.cnsns.2010.02.003.

36. Makinde OD, Aziz A. Boundary layer flow of a nanofluid past a stretching sheet with a convective boundary condition. Int J Therm Sci. 2011;50(7):1326–32. doi:10.1016/j.ijthermalsci.2011.02.019.

37. Raptis A, Perdikis C. Viscous flow over a non-linearly stretching sheet in the presence of a chemical reaction and magnetic field. Int J Non Linear Mech. 2006;41(4):527–9. doi:10.1016/j.ijnonlinmec.2005.12.003.

38. Li FL, Wu ZK, Ye CR. A finite difference solution to a two-dimensional parabolic inverse problem. Appl Math Model. 2012;36(5):2303–13. doi:10.1016/j.apm.2011.08.025.

39. Kerdid N, Arif MS, Nawaz Y, Abodayeh K. Computational analysis of radiation effects in Williamson fluid flow through a porous medium under an inclined magnetic field. J Radiat Res Appl Sci. 2025;18(2):101499. doi:10.1016/j.jrras.2025.101499.

40. Farooq U, Kerdid N, Nawaz Y, Arif MS. High accuracy simulation of electro-thermal flow for non-Newtonian fluids in BioMEMS applications. Comput Model Eng Sci. 2025;144(1):873–98. doi:10.32604/cmes.2025.066800.